Asteroseismology and next generation stellar models - EES2014
C. Charbonnel, B.Dintrans, E.Michel
EAS Publications Series, Vol. ??, 2015

arXiv:1510.02651v1 [astro-ph.SR] 9 Oct 2015

OBSERVATIONAL TECHNIQUES TO MEASURE SOLAR AND STELLAR OSCILLATIONS

Rafael A. García[1]

Abstract. As said by Sir A. Eddington in 1925: "Our telescopes may probe farther and farther into the depths of space. At first sight it would seem that the deep interior of the sun and stars is less accessible to scientific investigation than any other region of the universe. What appliance can pierce through the outer layers of a star and test the conditions within?" Eddington (1926).
Nowadays, asteroseismology has proven its ability to pierce below stellar photospheres and allow us to "see" inside the interior of thousands of stars down to the stellar cores, answering the question asked by Eddington ninety years ago. In this chapter we review the general properties of the spectral analysis which is the base of any asteroseismic investigation. After describing the stellar power spectrum, we will describe in details the characterization of the modal spectrum. This chapter will end by a brief description of the instrumentation in both helio and asteroseismology.

Contents

1 Introduction **2**
1.1 Helio and asteroseismology 4
1.2 Type of oscillation modes 4
1.2.1 Acoustic modes 6
1.2.2 Gravity modes 7
1.2.3 Mixed modes 8

2 Spectral analyses **9**
2.1 Examples of common Fourier transform pairs 10
2.2 Some properties of the Fourier transform 13
2.2.1 The addition theorem 13
2.2.2 The shift theorem 13
2.2.3 The scaling (or similarity) property 13

[1] Laboratoire AIM, CEA/DSM – CNRS - Univ. Paris Diderot – IRFU/SAp, Centre de Saclay, 91191 Gif-sur-Yvette Cedex, France

© EDP Sciences 2015
DOI: (will be inserted later)

2.2.4 The convolution function . . . 14
2.2.5 Cross-correlation and autocorrelation . . . 14
2.2.6 The Rayleigh's (Parseval) theorem . . . 15
2.2.7 Shannon's or sampling theorem . . . 16
2.3 Real observations . . . 16
2.3.1 Sampling rate and Nyquist frequency . . . 16
2.3.2 Finite observations . . . 18
2.4 The discrete Fourier Transform . . . 20
2.5 Power Spectrum: Fast Fourier Transform . . . 22
2.5.1 Case of unevenly distributed points: Lomb-Scargle Periodogram . 23
2.6 Regular gaps in the time series . . . 24
2.7 Precision and detectability of modes . . . 29
2.8 Other Periodogram estimators . . . 30
2.8.1 Average Power Spectrum . . . 31
2.8.2 Multitaper spectral analysis . . . 31
2.8.3 Average Cross Spectrum: Temporal and Spatial . . . 32

3 Preparing the time series 34

4 The observed stellar power spectrum 36
4.1 Generalities . . . 36
4.2 Global oscillation parameters: $\Delta\nu$ and $\nu_{\max}$ . . . 36
4.3 The échelle diagram . . . 39

5 Characterizing the p-mode spectrum 40
5.1 Modeling the acoustic spectrum . . . 41
5.2 Extraction of mode parameters . . . 42
5.2.1 Helioseismology . . . 42
5.2.2 Asteroseismology . . . 44
5.3 Background fitting . . . 45
5.4 The solar p-mode spectrum as seen by GOLF and VIRGO/SPM . . . 46
5.5 Ensemble stellar p- and mixed-mode fitting . . . 49

6 Instrumentation 52
6.1 Helioseismic Doppler velocity instruments . . . 54
6.2 Helioseismic photometric observations . . . 55
6.3 Stellar instrumentation . . . 56
6.3.1 CoRoT . . . 56
6.3.2 *Kepler* . . . 58
6.4 Comparison between Doppler velocity and Intensity measurements . . . 59

1 Introduction

For a long time, investigations of stellar interiors have been restricted to theoretical studies only constrained by observations of their global properties and external characteristics.

However, in the last few decades the field has been revolutionized by the ability to perform seismic investigations of the internal properties of stars. Not surprisingly, it started with the Sun, where helioseismology (the seismic study of the Sun, e.g. Gough et al. 1996; Christensen-Dalsgaard 2002a) has been yielding information competing with what can be inferred about the Earth's interior from geoseismology.

The last few years have witnessed the advent of asteroseismology (the seismic study of stars, e.g. Bedding & Kjeldsen 2003), in particular for solar-like pulsators, thanks to a dramatic development of new observing facilities providing the first reliable results on the interiors of distant stars similar to the Sun. The coming years will see a huge development in this field.

Helio- and asteroseismology provide unique tools to infer the fundamental stellar properties (e.g., mass, radius, sound speed...) and to probe the internal conditions inside the Sun and stars (e.g. Stello et al. 2009). Today, asteroseismology also provides invaluable information to other scientific communities. As an example, it can give a good estimate of the masses, radii, and ages of the stars hosting planets (e.g. Bazot & Vauclair 2004; Bazot et al. 2005; Soriano & Vauclair 2010; Moya et al. 2010; Christensen-Dalsgaard et al. 2010; Gaulme et al. 2010; Batalha et al. 2011; Vauclair 2011; Borucki et al. 2012; Howell et al. 2012; Huber et al. 2013; Campante et al. 2015; Silva Aguirre et al. 2015), as it has been demonstrated for example comparing with stars for which Hipparcos parallaxes, spectroscopy and asteroseismology is available (Silva Aguirre et al. 2012). This is a key-information to understand the formation of these planetary systems and their evolution, and to constrain the habitable zones of the surrounding exoplanets that can also be influenced by the magnetic activity of the host stars (e.g. Mosser et al. 2005, 2009a,b; Karoff et al. 2009; García et al. 2010; Metcalfe et al. 2010; Poppenhaeger & Schmitt 2011; Basri et al. 2013; Mathur et al. 2013b, 2014a,b). Asteroseismology can also be used to determine if a star belongs to a cluster (Stello et al. 2011) and to verify cluster's properties (Basu et al. 2011; Corsaro et al. 2012). Asteroseismology leads to the testing and revision of our theories of stellar structure, dynamical processes, and evolution. Helio- and asteroseismology are today in a blooming phase both in their goals and in impact. Helioseismology has shown the way to asteroseismology, which is reaching its maturity thanks to the path opened by the CNES CoRoT satellite (Convection, Rotation and planetary Transits, Baglin et al. 2006), the NASA's *Kepler* spacecraft (Borucki et al. 2010; Koch et al. 2010) –and its extended mission K2 (Howell et al. 2014)–, the BRITE-Constellation of nanosatellites for precision photometry of Bright Stars (Weiss et al. 2014), and the future missions such as NASA's TESS (Transiting Exoplanet Survey Satellite, Ricker et al. 2014) and the ESA's M3 PLATO mission (Rauer et al. 2014). It is important to remember the pioneers of this research done thanks to some episodic ground-based campaigns (e.g. Stello et al. 2007; Bedding et al. 2010) and some solar-like oscillating stars observed from space using both, the American satellite WIRE (Wide-Field Infrared Explorer, Buzasi et al. 2000) and the Canadian MOST satellite (Microvariability and Oscillations of Stars, Matthews et al. 2000).

1.1 Helio and asteroseismology

Helio and asteroseismology aim at studying the internal structure and dynamics of the Sun and other stars by means of their resonant oscillations (e.g. Gough 1985; Turck-Chièze et al. 1993; Christensen-Dalsgaard 2002a, and references therein). These vibrations manifest themselves in small motions of the visible surface of the star and in the associated small variations of stellar luminosity. Variable stars can be found all across the Hertzsprung-Russell, H-R, diagram.

During the last 30 years, helioseismology has proven its ability to study the structure and dynamics of the solar interior in a stratified way. These seismic tools allow us to infer some physical quantities as a function of the radius and latitude: the sound-speed profile (e.g. Basu et al. 1997; Turck-Chièze et al. 1997), the density profile (e.g. Basu et al. 2009), the internal rotation profile in the convective zone (e.g. Thompson et al. 1996) and the radiative zone (e.g. Chaplin et al. 1999a; Couvidat et al. 2003; Eff-Darwich et al. 2008; Eff-Darwich & Korzennik 2013; Elsworth et al. 1995; García et al. 2004, 2008c) or the conditions and properties of the solar core (e.g. Appourchaux et al. 2010; Basu et al. 1997, 2009; García et al. 2007, 2008a,b; Turck-Chièze et al. 2001, 2004) are some well-known examples. Moreover, thanks to the detailed study of these variables, the position of the base of the convection zone (e.g. Christensen-Dalsgaard et al. 1985) or the Helium abundances (e.g. Vorontsov et al. 1991) are some examples of what has been inferred. These observational constraints have significantly improved the standard solar models.

The Sun, because of its proximity, has been a fundamental calibrator of stellar evolution but observations of many other stars (e.g. Chaplin et al. 2011c; Huber et al. 2011) –covering a larger region of the H-R diagram through asteroseismology– will allow testing stellar structure, evolution, and dynamo theories under many different conditions (e.g. Christensen-Dalsgaard & Houdek 2010). In this case, due to the absence of spatial resolution in the observations, only low-degree modes (those with a small number of nodal lines on the surface of the star, see Fig. 1) will be accessible. Therefore compared to the Sun, less detailed information will be available on stellar interiors.

Stars are also known to be magnetic rotating objects. Such dynamical factors, magnetism and rotation, affect the internal structure and evolution of stars (e.g. Brun et al. 2004; Zahn et al. 2008; Duez et al. 2010; Eggenberger et al. 2010), and modifies the observed spectrum. High precision observations provided by modern facilities (from ground-based or spaceborne instruments) allow to constraint these dynamical process with a precision never achieved before.

1.2 Type of oscillation modes

The quest to improve our knowledge of the structure and dynamics of the solar interior has been possible thanks to the study of the resonant modes that are trapped in its interior and their comparison with stellar models. The difference between the two provides valuable information on the errors and omissions of the theoretical models. Before describing and interpreting the observed spectra, it is important to have some basic knowledge of the properties of the waves we want to characterize.

The theory behind stellar oscillations is very well known and it has been longly

described by several authors (e.g. Cox 1980; Unno et al. 1989; Christensen-Dalsgaard 2002b). Without going into deep details, a brief review of some magnitudes and theoretical concepts that will be used in the rest of the manuscript are given here.

Solar-like oscillations are standing waves characterized by three integers: n, ℓ, and m (see Fig. 1). n is the radial order indicating the number of nodal shells along the radius, and it is an integer greater than zero. By convention, we denote the p modes by positive numbers and g modes by negative ones. The angular degree, ℓ, is an integer greater or equal zero that denotes the number of nodes in the surface of the sphere. The first ones usually receive special names. Thus, modes with ℓ=0 are called radial modes while those with $\ell \geq 1$ are the non-radial modes. Moreover, those modes with ℓ=1 are called dipole modes, those with ℓ=2 are the quadrupole modes and finally the ℓ=3 are the octupole modes. Finally, m is the azimuthal order and gives the number of nodal lines passing through the poles. It can take values from $-\ell$ to $+\ell$ passing by zero. For each eigenmode we can define a characteristic frequency $\nu_{n,\ell,m} = \omega_{n,\ell,m}/2\pi$.

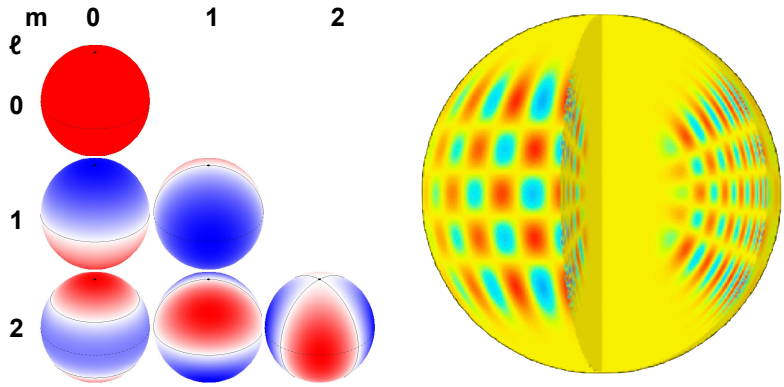

Fig. 1. Left: Example of spherical harmonics of degree ℓ=0,1,2 and azimuthal order m=0, 1, 2. The blue regions are those coming close to the observer, while the red regions represent those that are moving away. Right: Mode ℓ=20, m=16 and n=14.

Since the solar rotation lifts the azimuthal degeneracy of the resonant modes, their eigenfrequencies, $\nu_{n\ell m}$, are split into their $2\ell + 1$ m-components that are usually called the mode multiplet or simply multiplet. The frequency separation between two consecutive components is usually called rotational splitting (or just splitting) and it depends on the rotation rate in the region sampled by the mode. In the same way, the precise frequency of a mode depends on the physical properties of the cavity where the mode propagates. Using inversion techniques the rotation rate, the sound speed or the density profile at different locations inside the Sun can be inferred from a suitable lineal combination of the measured modes.

When we observe the Sun or the stars without any spatial resolution only low-degree modes ($\ell \leq 5$) can be observed. This is because for higher degree modes the regions with positive and negative velocities cancel out.

In the interior of solar-like stars we can define two main types of oscillations modes: the acoustic and the gravity modes.

1.2.1 Acoustic modes

Pressure driven modes (or p modes) are acoustic waves for which the restoring force arises from the pressure gradient. In the case of the Sun, the modes that are excited with the highest amplitudes are around the 3300 μHz producing the so-called 5-minutes oscillation of the Sun. They were first detected by Leighton et al. (1962), but interpreted as being part of the turbulent motions of the Sun. Tracing back the history of helioseismology (for a full review on the history of helioseismology see e.g. Chaplin 2006), the same year Evans & Michard (1962) confirmed the existence of the previous detection but it was not until 1970 when these oscillations were explained as standing waves trapped between the photosphere and the solar interior (Ulrich 1970; Leibacher & Stein 1971), with a particular relationship between the frequency and horizontal wave number. This explained the peaks or bands that appeared in a "diagnostic diagram" around 3 mHz, or 5 minutes (Tanenbaum et al. 1969; Deubner 1975). Subsequently, (Musman 1974) concluded that there was no spatial correlation between turbulent convection and the oscillatory waves, giving final independence to both events. Deubner (1975) confirmed experimentally the existence of eigenmodes, finding a relationship between the period and horizontal wavelength consistent with the predictions done by (Ulrich 1970). While previous observations showed evidences of spatially-localized oscillations in the solar atmosphere, Hill et al. (1975) announced the detection of oscillations in the solar diameter, suggesting the existence of global oscillations and, consequently, the possibility to use these pulsations to probe the solar interior (e.g. Scuflaire et al. 1975; Christensen-Dalsgaard & Gough 1976). This theoretical developments were confirmed by the detection of the p-mode power spectrum of the 5 minutes oscillations reported by Claverie et al. (1979) confirming the existence of global modes. These observations were then improved by Grec et al. (1980) thanks to the measurements obtained during 120 continuous hours from the South Pole, which sensibly improved the overall quality of the spectrum by reducing the daily aliases. The helioseismology, as we know it today was officially born.

Without going into the details of the theory behind the stellar oscillations, we can describe some useful characteristics. Therefore, while p modes propagate[1] inside the stellar interior, the sound speed increases and the waves are refracted. The deepest layer reached by the modes has a radius usually called the internal turning point, r_t which is defined by:

$$r_t = c_t\, L/(2\pi\nu_{n\ell})$$

where $L = \ell + 1/2$, $\nu_{n\ell}$ is the frequency of the mode, and $c_t = c(r_t)$ the sound-speed at the radius r_t (see for example Lopes & Turck-Chièze 1994).

Therefore, the internal turning point rises when the degree ℓ of the modes increases (see Fig. 2). For example, radial modes in the Sun will propagate all along the radius and cross the center. Dipole modes will have internal turning points in a range 0.04 to 0.1 $R_\odot$,

[1] Rigorously, waves propagate while eigenmodes do not.

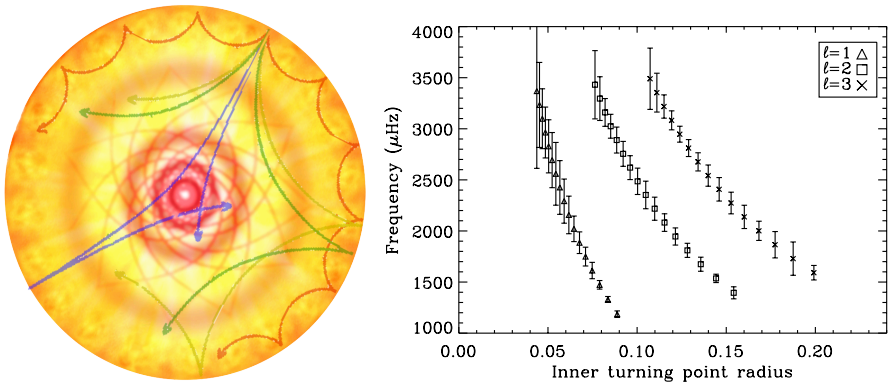

Fig. 2. Left: Representation of the solar interior with the radiative and the convective zones. Gravity modes can only propagate inside the radiative zone. Low-degree acoustic modes can propagate through most of the Sun (blue and green lines). High-degree modes only propagates in the outer layers of the Sun (orange lines). Right: Fractional radii of the Inner turning point for low-degree acoustic modes obtained from GOLF (García et al. 2008c). The error bars are the splitting error bars in nanohertz magnified by a factor of 10^4.

while octupole modes will propagate above 0.1 $R_\odot$. Moreover, for a fixed ℓ, the modes with increasing frequencies – higher radial order n – penetrate deeper inside the Sun (see right panel in Fig. 2).

Acoustic modes of the same degree are equidistant in frequency (in the asymptotic regime) which allows to define some global parameters of the p-mode pattern, such as the large and the small frequency separations (a detailed explanation of these quantities can be found in Mosser's chapter in this volume).

1.2.2 Gravity modes

For gravity modes (g modes) the restoring force is buoyancy. These modes propagate in the radiative interiors but they become evanescent in the convective zones reaching the surface of the Sun –and other stars with a thick outer convective zone– with very small amplitudes. This complicates their detection (see left panel in Fig. 2). These modes are located at lower frequencies compared to the p modes. In the case of the Sun, they have frequencies below $\sim$ 470 μHz and there are no ℓ=0 g modes. The frequency of g modes decreases with n. In the asymptotic regime, g modes are equidistant in period and not in frequency, with a very dense spectrum when going to higher periods (lower frequencies).

Figure 3 shows the separations in Period, ΔP_ℓ, between consecutive radial orders (n, n + 1) gravity modes of the Sun for ℓ= 1, 2, and 3 (red, green, and blue, respectively), using the theoretical frequencies from the seismic model (Mathur et al. 2007). The constant periodicity is achieved at 6, 4, and 2 hours for the modes ℓ = 1, 2, and 3, respectively. The g modes are split in frequency due to the rotation. They are very sensitive to the dynamics inside the radiative core (Mathur et al. 2008). To make the plot we have assumed a rigid

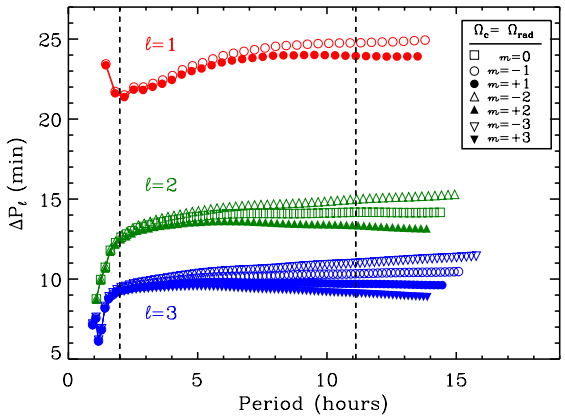

Fig. 3. g-mode period separations for modes with ℓ=1, 2 and 3 expressed in minutes versus the period of each gravity mode expressed in hours and assuming a rigid rotation rate in the radiative interior. See the text for details.

rotation in the Sun in which Ω_c is the angular velocity of the solar core, and $\Omega_{rad} \simeq 433$ nHz, is the angular frequency of the remaining radiative zone, and m is the azimuthal order of the modes. Inside the zone limited by the two vertical dashed lines (from ~ 2 to ~ 11 hours, corresponding to 25 to 140 mHz), we expect periodicities between 21 and 24 min for the dipole modes, between 12 and 14 min for the quadrupole modes, and between 9 and 11 min for the octupole modes.

1.2.3 Mixed modes

The distinction between pure acoustic modes and pure gravity modes is not always clear and sometimes they can be coupled together as it has already been described theoretically in previous works (e.g. Osaki 1975; Dziembowski & Pamyatnykh 1991; Christensen-Dalsgaard 2004; Dupret et al. 2009, and references there in). In such cases, we name these waves as mixed modes. Mixed modes are very interesting because they propagate as pressure waves in the convective envelope, and as gravity waves in the radiative interior. Therefore, they can probe the very inner core, while having enough amplitude in the surface to be detectable. The first observations of mixed modes in solar-like stars were reported from ground-based observations of η Boo, by Kjeldsen et al. (1995) and confirmed later by Kjeldsen et al. (2003), and Carrier et al. (2005). They were in very good agreement with theoretical predictions by e.g. Christensen-Dalsgaard et al. (1995).

Latter many observations of mixed modes have been done from ground-based observations but also from space thanks to CoRoT (e.g. Deheuvels et al. 2010) and *Kepler* observations (Chaplin et al. 2010; Campante et al. 2011; Mathur et al. 2011a). Beck et al. (2011) first reported the existence of mixed modes in red-giant stars. Latter, Bedding et al. (2011) and Mosser et al. (2011) showed the power of these modes to measure the evolu-

tionary status of red giants, with a clear difference between stars ascending the red-giant branch (RGB) and those in the clump.

2 Spectral analyses

The natural domain to analyze the information embedded in the rich spectrum of the Sun and the stars is through the Fourier spectrum. Let's start with some general definitions.

A signal, $f(t)$, is periodic of period T_0, if there is a period $T_0 > 0$ such as $f(t + T_0) = f(t)$ for all t. In this case, every integer number n of the fundamental period T_0, is also a period: $f(t + nT_0) = f(t)$, with $n = 0, \pm1, \pm2, ...4$. In the Fourier domain, the frequency associated to T_0, $1/T_0$, is called the fundamental frequency or the first harmonic of the signal. Any integer multiple of the fundamental frequency, $n/(T_0)$, with $n > 1$, is called and overtone or the 2nd harmonic (if $n = 2$), 3rd harmonic (if $n = 3$), etc. Examples of periodic functions are Sin(t) and cos(t). An example of a periodic function is given in Fig, 4.

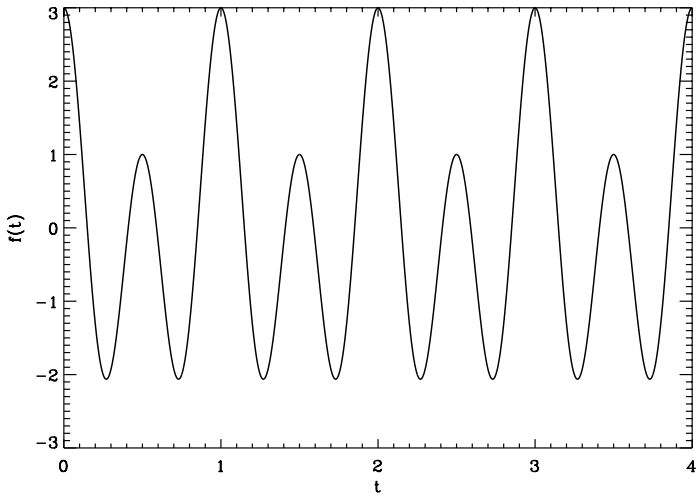

Fig. 4. Example of a periodic function $f(t) = \cos(2\pi t) + 2\cos(4\pi t)$.

In 1822 Joseph Fourier established the basis of the spectral decomposition by demonstrating that any arbitrary function can be decomposed in a combination of sine and cosine functions (i.e. harmonic functions). Therefore, it was established that for a given function $f(t)$, fulfilling the necessary conditions of continuity and finiteness, its continuous Fourier transform of an infinite time series $f(t)$ could be defined as:

$$\overline{f(t)} = F(\nu) = \int_{-\infty}^{\infty} f(t)\, e^{-2\pi i \nu t} dt \ , \tag{2.1}$$

where $i^2 = -1$. In general, the Fourier transform $F(\nu)$ is a complex function.

Apart from the sign of the exponential, the Fourier transform is its own reverse:

$$f(t) = \int_{-\infty}^{\infty} F(\nu)\, e^{2\pi i \nu t} d\nu \ , \tag{2.2}$$

which is usually called the reversed or inverse transform. Using the compact notation we have:

$$\overline{\overline{f(t)}} = \overline{F(\nu)} = f(t) \ . \tag{2.3}$$

2.1 Examples of common Fourier transform pairs

Each combination of a function $f(t)$ and its Fourier transform $F(\nu)$ is usually called a Fourier transform pair. In this section we are going to review some Fourier transform pairs usually found in the analysis of real seismic data. For a complete review on Fourier transforms and Fourier transform pairs please refer to Bracewell (2000).

- $f(t)$= constant ; $F(\nu)$ is a Dirac delta (see Fig. 5):
  $F(\nu) = \delta(\nu)$.

- $f(t) = cos(at)$; $F(\nu)$ are two Dirac deltas centered at $\pm a$ (see Fig. 6):
  $F(\nu) = \delta(\nu - a) + \delta(\nu + a)$.

  That implies that for sinusoidal signals, $F(\nu)$ is only different from zero at $\nu = \pm\nu_a$. Therefore, in the case of multi periodic signals (defined as the superposition of several sinusoidal functions) of frequencies ν_1,..., ν_N, and amplitudes A_1, ..., A_N, its Fourier transform, $F(\nu)$, can be written as a sum of harmonic functions with:

  $$\overline{f(t)} = F(\nu) = \sum_{k=1}^{N} A_k \delta(\nu - \nu_k) \quad . \tag{2.4}$$

- $f(t)$ = Boxcar function of width a ; $F(\nu)$ is a Sinc function of width at half maximum 1/a (see Fig. 7):
  $F(\nu) = 2a\ \mathrm{sinc}(a\nu\pi) = 2a\ \sin(a\nu\pi)/a\nu\pi$.

- $f(t)$ = Gaussian of width a: $f(t) = e^{-t^2/2a^2}$; $F(\nu)$ is another Gaussian (see Fig. 8):
  $F(\nu) = (2\pi)^{1/2} a e^{-(a\nu)^2/2}$.

- $f(t)$= Exponential, $f(t) = e^{-|t|}$; $F(\nu)$ is a Lorentzian function (see Fig. 9):
  $F(\nu) = 2/(1 + (2\pi\nu)^2)$.

- $f(t)$= Dirac Comb function defined as a series of Dirac deltas separated by dt, $f(t) = \mathrm{III}_{\mathrm{dt}}(\mathrm{t}) = \sum_{\mathrm{k}=-\infty}^{\infty} \delta_{\mathrm{kdt}}$; $F(\nu)$ is another Dirac Comb function but spaced $1/dt$ (see Fig. 10):
  $F(\nu) = \mathrm{III}_{1/\mathrm{dt}}(\nu)$.

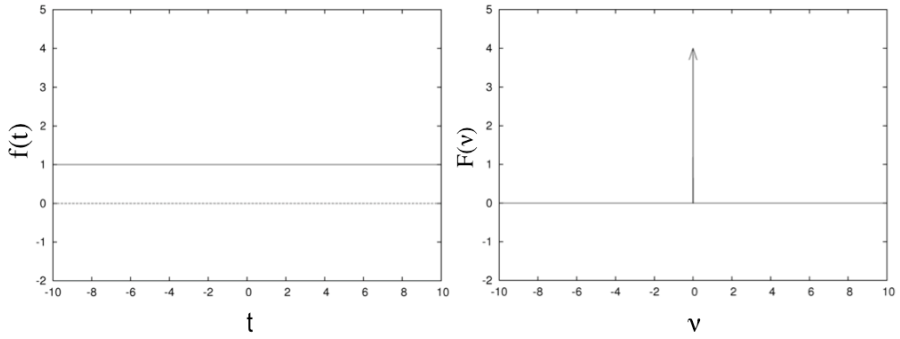

Fig. 5. Fourier Transform pair of a constant and a Dirac function.

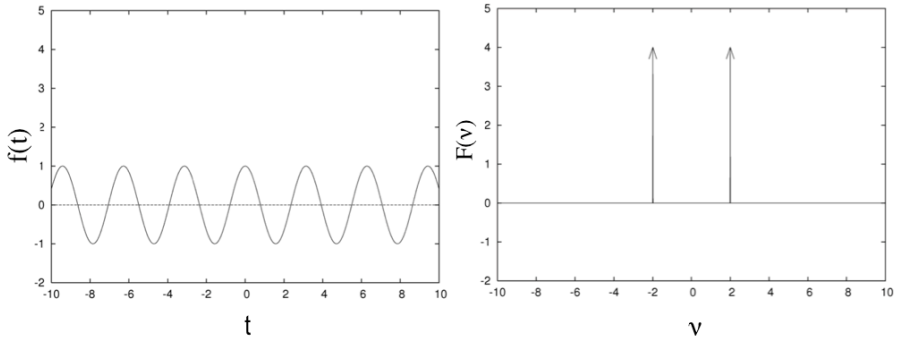

Fig. 6. Fourier Transform pair of a cosinus function and a pair of Dirac deltas.

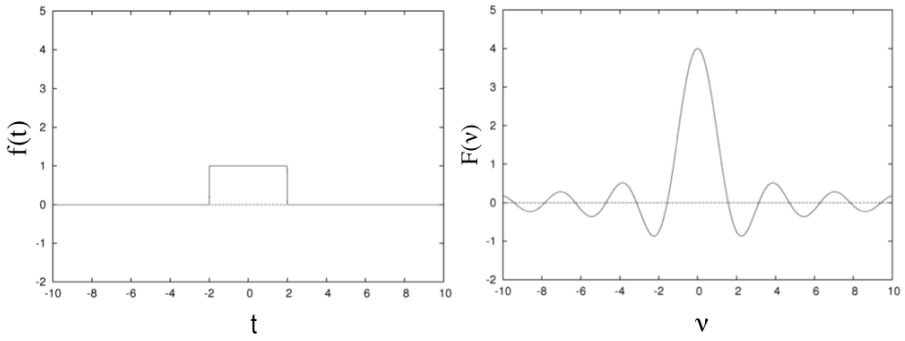

Fig. 7. Fourier Transform pair of a boxcar function and a sinc.

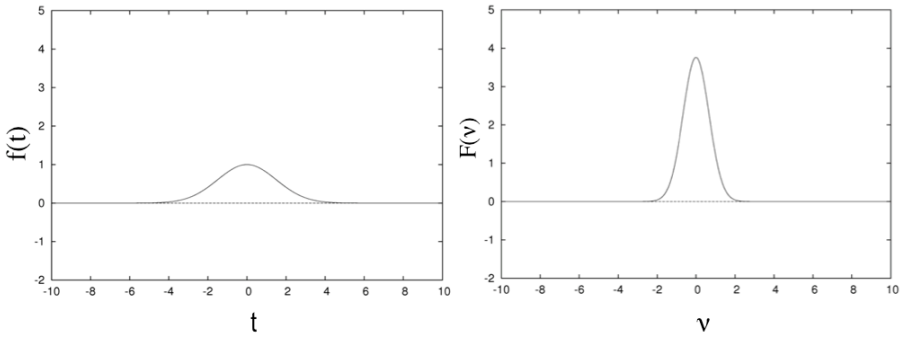

Fig. 8. Fourier Transform pair of a Gaussian function.

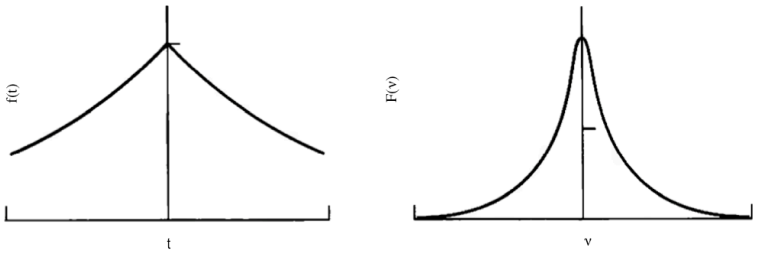

Fig. 9. Fourier Transform pair of a exponential and a Lorentzian function.

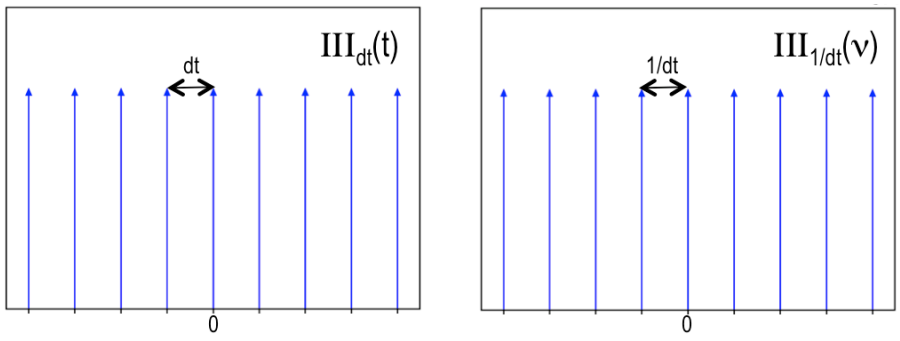

Fig. 10. Fourier Transform pair of a Comb function.

2.2 Some properties of the Fourier transform

2.2.1 The addition theorem

The Fourier Transform is a linear transformation. Hence, given two functions $f(t)$ and $g(t)$, whose Fourier Transforms are $F(\nu)$ and $G(\nu)$, respectively, the Fourier Transform of any linear combination of $f(t)$ and $g(t)$ is:

$$\overline{h(t)} = \overline{af(t) + bg(t)} = aF(\nu) + bG(\nu) \tag{2.5}$$

where a and b are any real or imaginary constants.

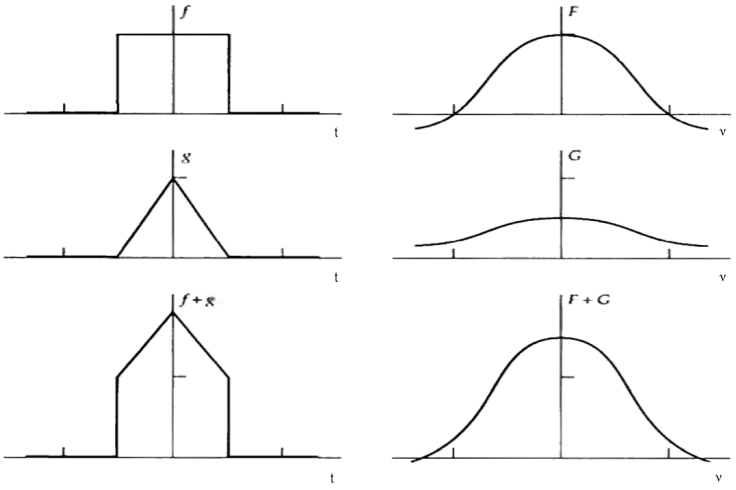

Fig. 11. Graphical illustration of the addition theorem (from Bracewell 2000).

2.2.2 The shift theorem

The Fourier transform of a function shifted in time by a real number a, is a function that does not change in amplitude but in phase:

$$\overline{f(t-a)} = e^{-2\pi i a\nu} F(\nu) \quad . \tag{2.6}$$

In other words, each Fourier component will be delayed by a factor which is proportional to the frequency ν, the higher the frequency, the greater the change in the phase angle. See a graphical illustration of the shift theorem in Fig. 12.

2.2.3 The scaling (or similarity) property

A compression of the time scale corresponds to the expansion of the frequency scale:

$$\overline{f(at)} = \frac{1}{a} F\left(\frac{\nu}{a}\right) \quad . \tag{2.7}$$

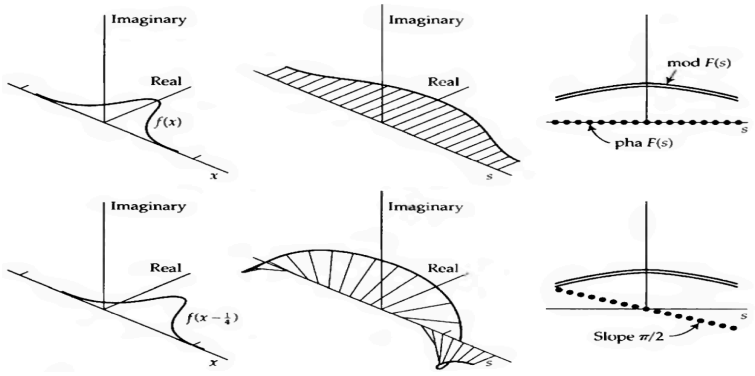

Fig. 12. Graphical illustration of the shift theorem (from Bracewell 2000).

However, as one member of the transform pair expands horizontally, the other not only contracts horizontally but also grows vertically. In such way, the area beneath the functions is preserved. For periodic signals, an expansion of a function in time corresponds to a stretching of the frequencies in the Fourier domain. In other words, a "wide" function in the time-domain is a"narrow" function in the frequency-domain. This is the basis of the uncertainty principle in quantum mechanics and the diffraction limits of radio telescopes.

2.2.4 The convolution function

The convolution function gives the area overlapped between the two considered functions, $f(t)$ and $g(t)$, as a function of the amount that one is translated in respect to the other one. In this case, u is the time lag between the two:

$$h(u) = f * g = \int_{-\infty}^{\infty} f(t)g(u-t)dt \quad . \tag{2.8}$$

To ensure commutability, the two functions move in opposite directions (see Fig. 14 for a graphical representation). It can be seen that the Fourier transform of the product of two functions is the convolution of the Fourier transform of each one:

$$\overline{fg} = \overline{f} * \overline{g} \tag{2.9}$$

2.2.5 Cross-correlation and autocorrelation

It is a measure of similarity of two waveforms as a function of a time lag applied to one of them (see Fig. 14 for a graphical representation):

$$h(u) = f \star g = \int_{-\infty}^{\infty} f^*(t)g(t+u)dt \quad . \tag{2.10}$$

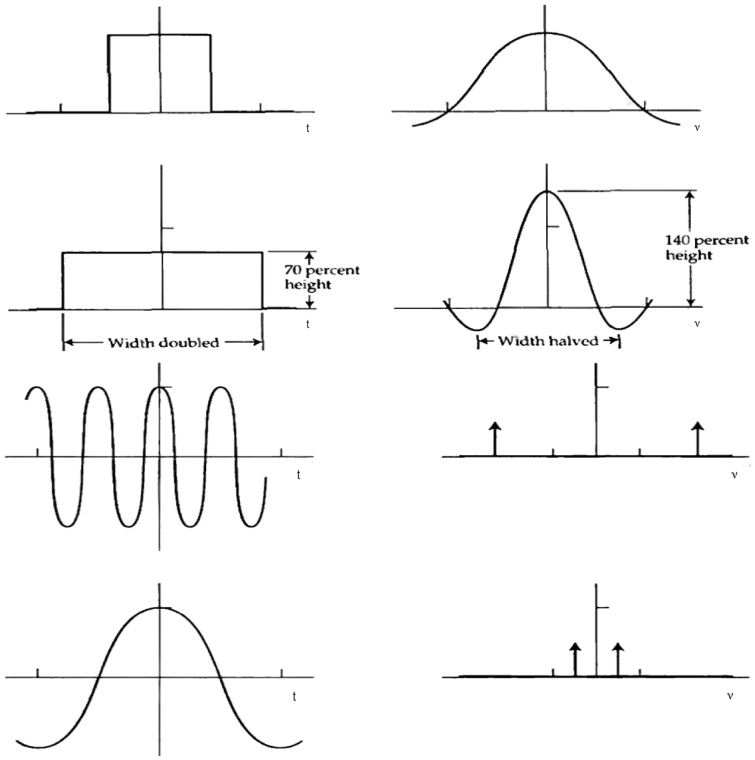

Fig. 13. Graphical illustration of the scaling theorem for two boxcar functions (upper two panels) and two cosinus functions (lower two bottom panels). From Bracewell (2000).

In the special case in which the cross-correlation is applied with the same function, it is called autocorrelation. It provides the linear dependence of a variable with itself at two points in time:

$$h(u) = g \star g = \int_{-\infty}^{\infty} g^*(t)g(t+u)dt \quad . \tag{2.11}$$

In this case, if a function g(t) has its Fourier transform $G(\nu)$ then the Fourier transform of its autocorrelation is $\mid G(\nu) \mid^2$.

The autocorrelation has always a maximum in zero. For stationary processes, the autocorrelation between any two functions only depends on the time lag between them (u).

2.2.6 The Rayleigh's (Parseval) theorem

The Rayleigh's theorem (applied for the first time by Lord Rayleigh in 1879 while investigating blackbody radiation), is sometimes also called the Plancherel's theorem (because

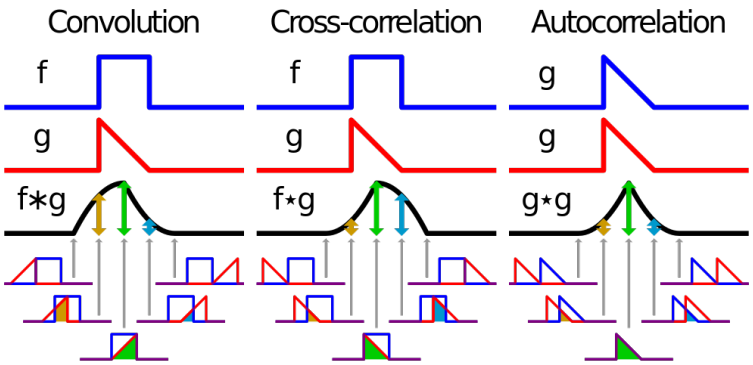

Fig. 14. Graphical comparison between convolution, cross-correlation and autocorrelation (credits Cmglee).

he established in 1910 the conditions under which it holds) and is related to the Parseval's theorem (1799) for Fourier series. It shows that the integral of the squared modulus of a function is equal to the integral of the modulus of its spectrum. In other words, it establishes that the energies in the time and frequency domains are equal:

$$\int_{-\infty}^{\infty} | f(t) |^2 \, dt = \int_{-\infty}^{\infty} | F(\nu) |^2 \, d\nu \ . \tag{2.12}$$

2.2.7 Shannon's or sampling theorem

In the case of a function with a limited spectral response (between $\nu_{\rm min}$ and $\nu_{\rm max}$), its sampling frequency should be $\Delta\nu > 2\nu_{\rm max}$. If the signal is periodic, to properly sample such function in the time domain, it is necessary that $\Delta t < T_o/2$. In other words, it is necessary to have more than two distinct points per fundamental period to properly sample the function. This theorem established the basis of the discretization.

2.3 Real observations

When dealing with observations of real physical phenomena, it is natural to start the observations at a given moment and perform the measurements during a given time at a given rate. Therefore, we need to set up the basis to move from a continuous mathematical description to a discrete framework which physicist usually deals with.

2.3.1 Sampling rate and Nyquist frequency

Let's assume that $f(t)$ is a band-limited signal, i.e., a signal whose Fourier transform is identically zero outside a finite interval (see panel (a) in Fig.15) .

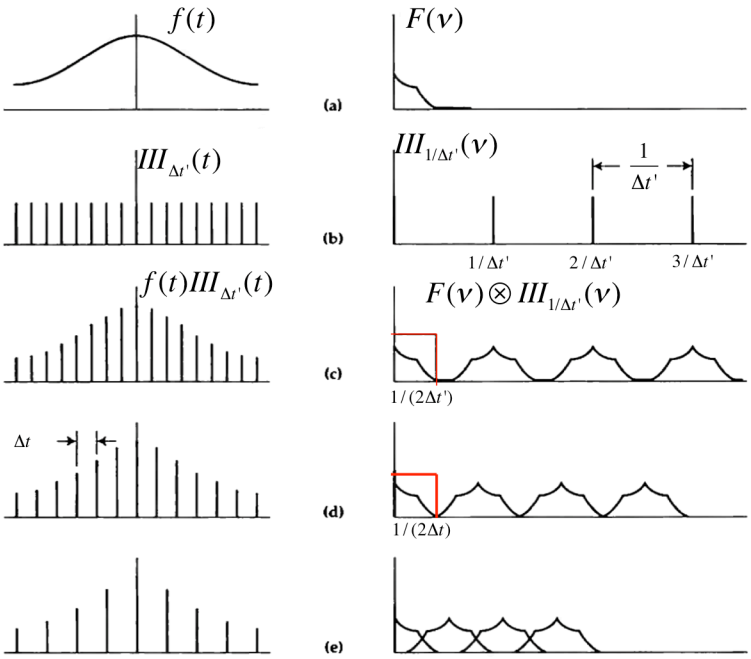

Fig. 15. Graphical representation of the discretization of a signal and the aliasing. (a) $f(t)$ is a band-limited signal whose Fourier transform $F(\nu)$ is zero outside a given interval. (b) $\mathrm{III}_{\Delta t'}$(t) is a Comb function of separation $\Delta t'$ whose Fourier transform is another Comb function of separation $1/\Delta t'$. It is used to discretize $f(t)$ by multiplying both functions in the temporal domain (c). The Nyquist frequency, $\nu_{\rm Nyquist} = 1/(2\Delta t)$, determines the longest sampling rate Δt that a band-limited signal can be measured (d). Panel (e) illustrates the case when the signal $f(t)$ is undersampled and the signal is aliased in the spectrum around the Nyquist frequency. Based on Bracewell (2000).

In this case, applying the Shannon's theorem, the signal $f(t)$ can be completely recovered if it is sampled with a rate $\Delta\nu > 2\nu_{\rm max}$.

Let's define a Comb function of separation $\Delta t'$ whose Fourier transform is another Comb function of separation $1/\Delta t'$ in such way that $1/\Delta t' > 2\nu_{\rm max}$ (see panel (b) in Fig.15). The process of measuring the signal $f(t)$ implies the discretization of the signal. If the measurement is done at a rate of $\Delta t'$ (the temporal resolution), then the measurement consists of multiplying the function $f(t)$ by de Comb function $\mathrm{III}_{\Delta t'}$(t). In the Fourier domain, the signal is represented by the convolution $F(\nu) * \mathrm{III}_{1/\Delta t'}(\nu)$. Hence, $F(\nu)$ is repeated at every multiple of $1/\Delta t'$ as illustrated in the panel (c) of Fig. 15. Because $f(t)$ is band-limited, $F(\nu)$ is a perfect representation of $f(t)$ if the sampling rate Δt is such that $\nu_{\rm max} = 1/(2\Delta t)$ (see Fig. 15 (d)). This high frequency cut-off of the system for a given sampling rate Δt is known as the Nyquist frequency, $\nu_{\rm Nyquist} = 1/(2\Delta t)$. For any sampling rate longer than the Δt mentioned above, the signal would be undersampled.

Any frequencies present in the original signal above $\nu_{\rm Nyquist}$ (also called super-Nyquist regime) will be reflected or *aliased* back into the frequency region below $\nu_{\rm Nyquist}$ mixing with the real signal lying in this region as illustrated in panel (e) of Fig. 15 (or further details on super-Nyquist seismology with *Kepler* see Murphy et al. 2013; Chaplin et al. 2014). As a consequence, if the signal $F(\nu)$ was band limited and it is sampled at a higher cadence than $\nu_{\rm Nyquist}$, no aliasing will appear in the spectrum in accordance to the Sampling Theorem.

2.3.2 Finite observations

Most of the physical processes in which seismology is interested in, correspond to signals that are not band limited. During the observing time, T, only part of the signal is sampled N times at a rate given by Δt: $f_N(t)$. Mathematically this is equivalent to multiplying a given infinite (or longer than the observations) signal sampled N times $f_N(t)$ by a *window function* represented by a square function, $\sqcap_T(t)$ defined as being 1 between the range $[-T/2, T/2]$ and zero elsewhere. Therefore, our observations can be represented as the product:

$$f(t)\,\mathrm{III}_{\Delta \mathrm{t}}(\mathrm{t})\ \sqcap_{\mathrm{T}}(\mathrm{t}) = \mathrm{f_N(t)}\ \sqcap_{\mathrm{T}}(\mathrm{t}) \quad . \tag{2.13}$$

An illustration can be seen in the top panel of Fig. 16 for an infinite Gaussian function sampled at Δt and observed during a time span of T.

Because the Fourier transform assumes that $f_N(t)$ is implicitly periodic, it is defined as follows $f(t)\mathrm{III}_{\Delta \mathrm{t}}(\mathrm{t})\sqcap_{\mathrm{T}}(\mathrm{t}) * \mathrm{III}_{\mathrm{T}}(\mathrm{t})$ (see middle panel in Fig. 16).

The Fourier transform $F_N(\nu) = \overline{f_N(t)}$ can then be defined as:

$$F_N(\nu) = \overline{f_N(t)} = F(\nu) * \mathrm{III}_{1/\Delta \mathrm{t}}(\nu) * \mathrm{sinc}(\nu)\,\mathrm{III}_{1/\mathrm{T}}(\nu) \quad . \tag{2.14}$$

An illustration of $F_N(\nu)$ can be seen in the bottom panel of Fig. 16. Each vertical line is in reality a Sinc function. For the sake of clarity, these Sinc functions have not been drawn. The function $F_N(\nu)$, has a frequency resolution $\Delta\nu = 1/T$ and has a Nyquist frequency of $1/(2\Delta t)$ as explained before. Because $f_N(t)$ is assumed to be periodic, $F_N(\nu)$ is also periodic at multiples of $1/\Delta t$. Moreover, there is an aliasing around the cut-off frequency because the function $f_N(t)$ is not band limited.

An example of the effect of the window size is shown in Fig. 17 for the *Kepler* red giant KIC 5356201 with $\nu_{\rm max} = 212\ \mu$Hz. When this star is observed during 100 days (typical length of observations of K2 and some CoRoT fields), only the rough characteristics of the modes can be observed and, for example, the splittings of the mixed modes cannot be measured. However, when the observations stands for 4 years, the fine structure of the multiplets in the mixed modes are clearly distinguishable, and a precise measurement of the core internal rotation can be obtained (Beck et al. 2012).

To properly resolve the rotational split components of a multiplet, as in Fig. 17, it is necessary to have enough frequency bins between the two maxima. This will depend on the rotation rate of the cavity traversed by the modes, but also on their line widths (e.g. Ballot et al. 2006). When the modes are stochastically excited (Lorentzian profile) it is commonly assumed that the length of the time series T needs to be 10 times longer than the mode lifetime τ (defined as the time for the amplitude to decay by the factor e,

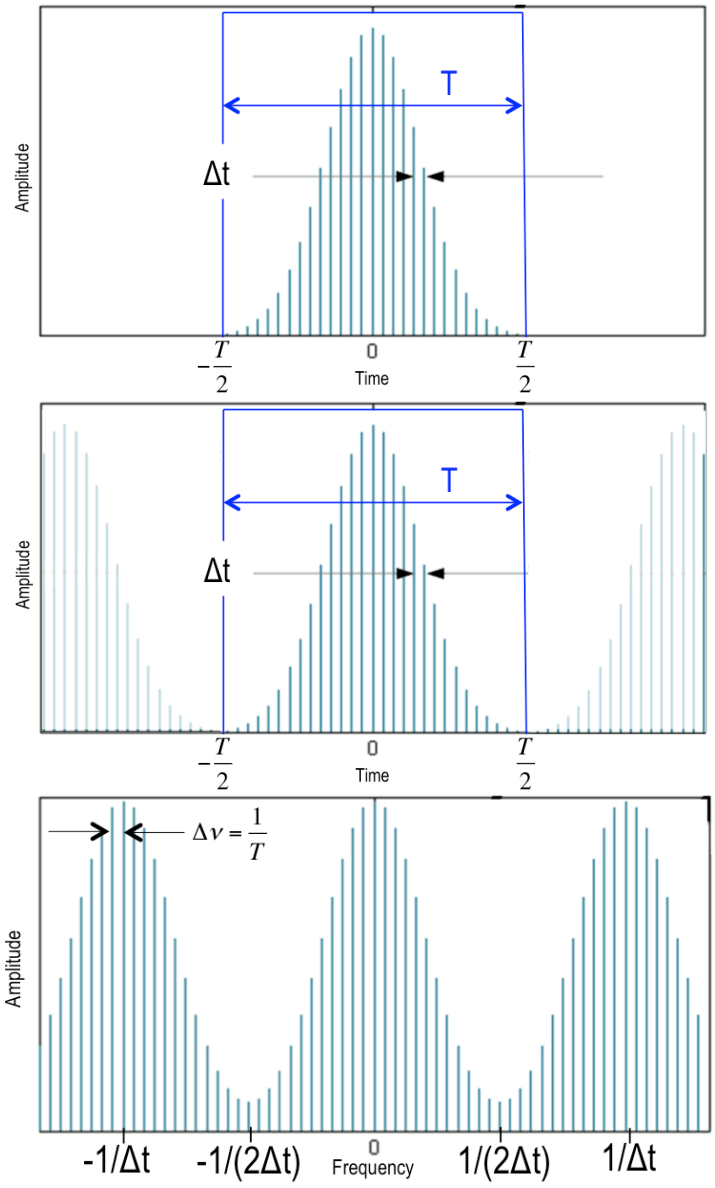

Fig. 16. Gaussian function, $f(t)$, observed at a sampling rate of Δt multiplied by a window function of width T (top panel). Because $f(t)$ is implicitly periodic (middle panel), $F(\nu)$ is sampled at a rate $1/T$. When $f(t)$ is not band limited, there is an aliasing around the Nyquist frequency in $F(\nu)$ (bottom panel).

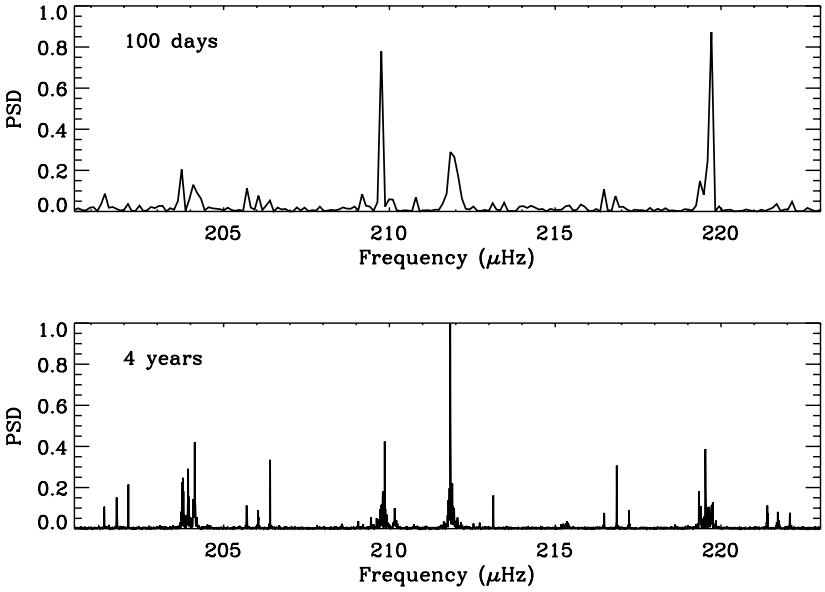

Fig. 17. Power density spectrum of the red giant KIC 5356201 observed by *Kepler*. On top, during 100 days, on the bottom panel, during the full length of the mission, 4 years.

$\tau = 1/(\pi\Gamma)$) in order to resolve the mode profile (Chaplin & Howe 2015; Appourchaux & Grundahl 2015). For example, for lifetimes of 3.7 days ($\Gamma = 1$ μHz, typical for main-sequence solar-like stars with $T_{\rm eff} = 5770$ K), the length of the observations required to properly characterize the modes is 37 days. It is also important to notice that when the ratio between the mode lifetime and the length of the observations is small ($T/\tau \leq 2$), the observed profile tends to a Sinc-squared function.

2.4 The discrete Fourier Transform

Following the concepts defined in the previous sections, it is possible to define the Discrete Fourier Transform (D.F.T.) as the finite sum of complex sinusoids, ordered by their frequencies, representing a regularly sampled temporal function:

$$D.F.T. = \overline{f(t_n)} = F_N(\nu_k) = \Delta t \sum_{n=1}^{N} f(t_n)\, e^{(-i2\pi\nu_k t_n)} \quad , \tag{2.15}$$

where $\nu_k = k/T = k\Delta\nu$, $t_n = n\Delta t$, and $T = N\Delta t$. This expression is equivalent to the truncated original Fourier series and it is implicitly periodic at $\Delta\nu = 1/\Delta t$, i.e., at frequencies double of the Nyquist frequency.

A particular interesting case is when the function $f(t)$ is periodic and it is observed during a period T which is an integer number of periods of the original signal. In such case, the zeroes of the sinc function in the Fourier transform coincide with the points used to compute the discrete Fourier transform and it can be approximated by a Dirac (in non oversampled power spectra, see Fig. 18).

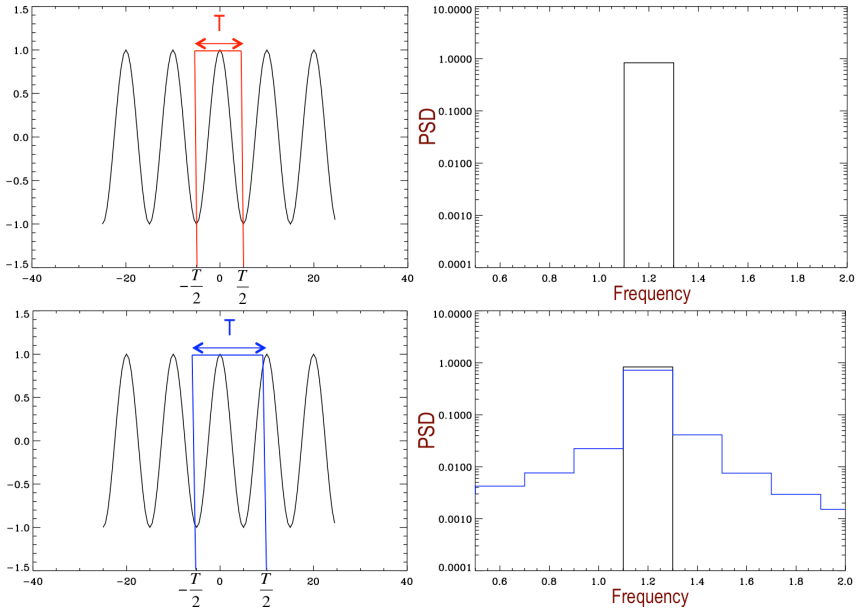

Fig. 18. Periodic function in the time domain (left-hand panels) observed during an integer number of periods (top) or with another observational length (bottom). The right hand-side panels correspond to the Fourier transform. In the first case, the Fourier transform is a sinc function in which the zeroes coincide with the points used to compute the discrete Fourier transform. It can be approximated as a Dirac. In the second case, it is a broad Sinc function (blue line in the bottom right-hand panel). To facilitate the comparison we have also overplotted the Sinc function of the previous case (in black).

An interesting consequence of the above is that the amplitude of a periodic signal with period P changes in the spectrum depending on the remainder of T/P. In the best case, when the reminder of this ratio is zero, T is proportional to the period of the signal and all the power will be concentrated in the central bin. However, when the remainder is bigger, the Fourier transform is a Sinc function and some power leaks into the adjacent bins while the central one is reduced. This should be taken into account when low-amplitude peaks are searched in a noisy spectrum. In such case, it can be interesting to oversample the signal or to slightly change T by removing some points of the temporal signal (e.g. Gabriel et al. 2002; Turck-Chièze et al. 2004).

It has been demonstrated that an oversampling of a factor of 6 (adding zeroes at the

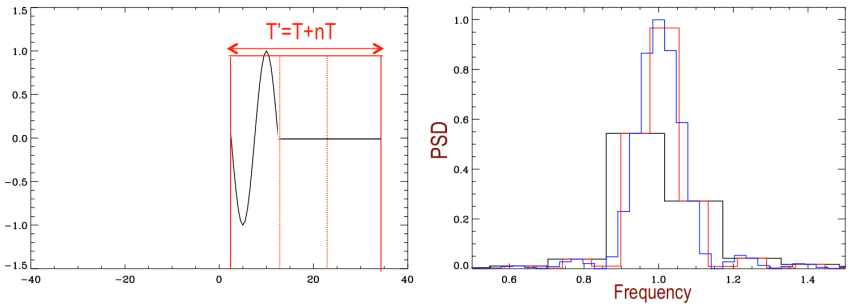

Fig. 19. Time series of a periodic signal (left panel) and corresponding Fourier transform (Sinc function in the right panel) for different zero padded time series $T + nT$, with n=0, 3, and 6; black, red, and blue courbes respectively.

end of the time series by 5 times the length of the series) the central bin of the Sinc function recovers ~ 97% of the total signal (for more details see Gabriel et al. 2002).

2.5 Power Spectrum: Fast Fourier Transform

It is common to work with the power spectrum instead of the amplitude spectrum. It is defined as the modulus squared of the Fourier transform:

$$\mid F_N(\nu_k) \mid^2 = P_N(\nu_k) = \frac{1}{N}\left\{\left(\sum_{n=1}^{N} f(t_n)\cos(2\pi\nu_k t_n)\right)^2 + \left(\sum_{n=1}^{N} f(t_n)\sin(2\pi\nu_k t_n)\right)^2\right\} \quad . \tag{2.16}$$

The power spectrum has no information on the phase of the original function. It is generally defined between $[0,\nu_{\rm Nyq}]$. When this is the case it is called "single-sided" power spectrum, in opposition to the "double-sided" power spectrum defined in the full range of frequencies between $[-\nu_{\rm Nyq}, \nu_{\rm Nyq}]$ (see also the extended discussion in Press et al. 1992). This has an impact on the calibration of the power spectrum. The proper way to calibrate the power spectrum is by applying the Parseval's Theorem (see Eq. 2.12), i.e., by ensuring that the integral of the squared modulus of the function in the time domain is equal to the integral of the squared of its spectrum. In the case of the single-sided power spectrum, the power of each bin is multiplied by two to take into account the power in the negative frequency region. In seismology it is very common to work with the power spectrum density (or PSD) which is the power spectrum divided by the resolution in the Fourier domain. This representation has the advantage that it takes into account the variable size of the frequency bin for different lengths of observations T, allowing simple and direct inter comparations between spectra computed from datasets of different lengths.

Assuming that $f(t)$ is normally distributed for $N >> 1$, then the real and imaginary parts will also be normally distributed. Therefore, the power spectrum will follow a χ^2 with 2 degrees of freedom statistics.

When the signal $f(t)$ is evenly sampled the sums involved in Eq. 2.16 requires N^2 operations. This can take quite some amount of time and several algorithms of *Fast Fourier Transform* have been developed to increase the speed. They usually require a number of operations that are of the order of $n \log N$ (see some examples in Press et al. 1992, and references therein).

2.5.1 Case of unevenly distributed points: Lomb-Scargle Periodogram

When the sampling rate is not regular and the data are unevenly distributed, the Fourier spectrum does not follow in the general case a χ^2 with 2 degrees of freedom statistics. To overcome this issue, Scargle (1982) developed the so-called Lomb-scargle (LS) periodogram:

$$F_{LS}(\nu_k) = \frac{1}{\omega(\tau)} \sum_{n=1}^{N} f(t_n) \cos(2\pi\nu_k(t_n - \tau)) + i\frac{1}{\nu(\tau)} \sum_{n=1}^{N} f(t_n) \sin(2\pi\nu_k(t_n - \tau)) \quad , \quad (2.17)$$

where:

$$\omega(\tau) = \sum_{n=1}^{N} cos^2(2\pi\nu_k(t_n - \tau)) \quad , \quad (2.18)$$

$$\nu(\tau) = \sum_{n=1}^{N} sin^2(2\pi\nu_k(t_n - \tau)) \quad (2.19)$$

and τ is selected to keep the invariant with time of equation Eq. 2.17 as follows:

$$\tan(2\pi\nu\tau) = \frac{\sum_{n=1}^{N} \sin(2\pi\nu t_n)}{\sum_{n=1}^{N} \cos(2\pi\nu t_n)} \quad . \quad (2.20)$$

With this formulation, it can be demonstrated that the power spectrum $\mid F_{LS}(\nu_k) \mid^2$ follows a χ^2 with 2 degrees of freedom statistics (Press & Rybicki 1989). The Lomb-Scargle periodogram implicitly adds zeroes at the positions of the missing points, which means that the bins are correlated as in any time series with gaps. It is also important to notice that to speed up the calculations the LS periodogram is sometimes approximated by an interpolation into a regular mesh of points and the use of a FFT algorithm properly normalized (Scargle 1982).

Unevenly sampled data, as the ones obtained by the *Kepler* satellite, can be useful to disentangle real peaks from aliases at frequencies close to the Nyquist cut-off frequency (Murphy et al. 2013). In Fig. 20 we show a series of pure sinusoids of unit amplitude with frequencies between 310 and 460 μHz above the Nyquist frequency and irregularly sampled following the *Kepler* timing (see more details on the *Kepler* timing in García et al. 2014b).

Because the sampling is not regular, the aliased peaks into the frequency band below $\nu_{\rm Nyq}$ are not perfect (see a zoom of the peaks marked "a, b, c, and d" in Fig. 21). As explained by Chaplin et al. (2014) the exact structure of the alias peaks is different and depends on the relation of their frequencies with the sampling frequency. For coherent pulsators (with narrow peaks), the detailed study of the sidebands in the peaks allows to

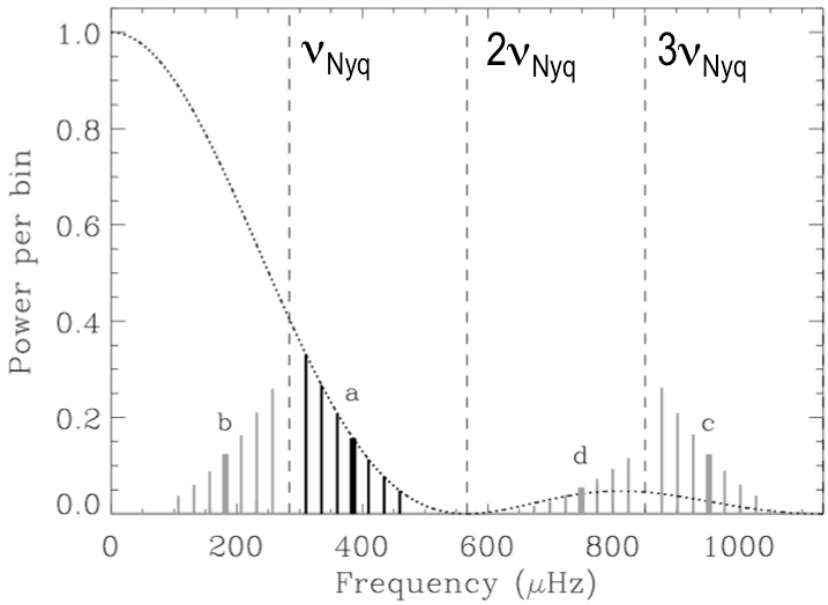

Fig. 20. Power Spectrum of a series of pure sinusoids of unit amplitude having frequencies between 310 and 460 μHz irregularly sampled in time. The black vertical lines are the true frequencies while the grey ones are the aliases. The dotted line marks the Sinc-squared attenuation envelope. See the discussion in the text about the general shape of the spectrum. The vertical dashed lines are the multiples of $\nu_{\rm Nyq}$. Adapted from Chaplin et al. (2014).

discriminate real peaks to the aliased ones (Murphy et al. 2013). However, in the case of solar-like pulsators with modes of short lifetimes, the situation is more complicated because the structure of the aliases is mixed with the natural stochastic excitation of the modes (Chaplin et al. 2014).

The general appearance of the full power spectrum is affected by the effective integration time per sampling unit used to collect the data (usually called cadence). Assuming an integration time per cadence of $\Delta t'$, the amplitude of any signal at a given frequency ν is given by $\eta = \mathrm{sinc}(\pi\nu\Delta\mathrm{t}')$ (Campante 2012). When the integration time is close to the sampling time (i.e., the dead time per measurement is close to zero), $\Delta t' \sim \Delta t$, the amplitudes follows the attenuation factor defined as $\eta = \mathrm{sinc}(\pi\nu/(2\nu_{\rm Nyq}))$ (e.g. Chaplin et al. 2014, and references therein).

2.6 Regular gaps in the time series

Continuous observations of real phenomena are usually difficult. In ground-based astronomy, the observation of the Sun and stars is conditioned by the rotation of the Earth. Thus, unless observing at high latitudes, it is generally impossible to observer longer than 10-15

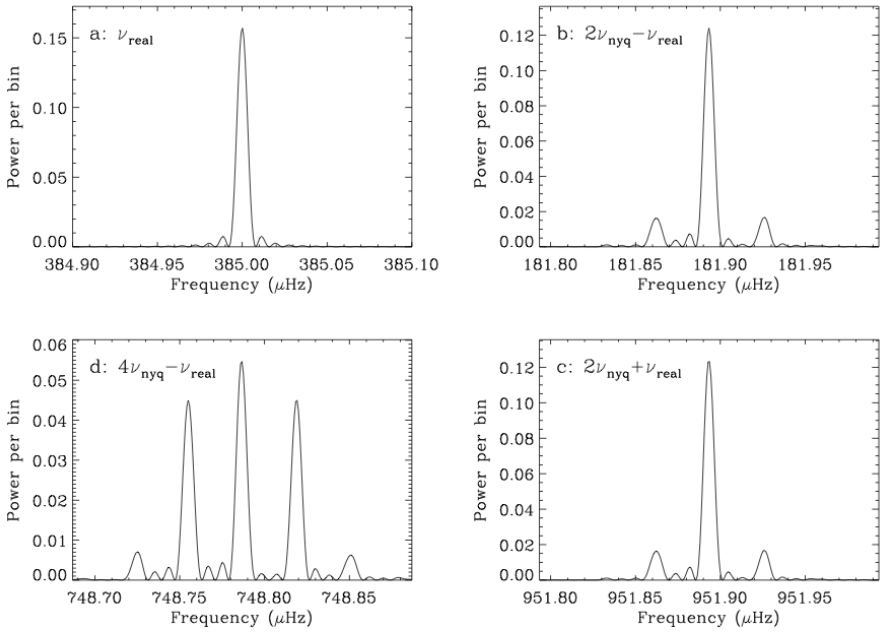

Fig. 21. Zoom of the Power Spectrum of the peaks marked "a, b, c, and d" in Fig. 20 (from Chaplin et al. 2014).

hours continuously the same object. In seismology, the existence of regular gaps in the data has ominous effects in the Fourier domain.

Short regular gaps in the time series can be represented mathematically as the product of the signal we are interested in, $f(t)$, with a Comb function of period T_1:

$$\overline{\mathrm{III}_{\mathrm{T}_1}(\mathrm{t})} = \mathrm{III}_{1/\mathrm{T}_1}(\nu) \tag{2.21}$$

In the case of longer gaps, the mathematical representation is a product of a rectangular window convolved with a Comb function:

$$\overline{\sqcap_{T_2}(t) * \mathrm{III}_{\mathrm{T}_1}(\mathrm{t})} = \mathrm{sinc}(\nu)\,\mathrm{III}_{1/\mathrm{T}_1}(\nu) \tag{2.22}$$

Due to the day-night alternance, ground-based seismic observations of a single site of the Sun or stars imply that each mode in the power spectrum will appear at frequencies multiples of 1/24 h, i.e., 11.57 μHz, usually called daily sidebands. In Fig. 22 the GOLF power spectrum density is shown. In the top panel the one obtained from 100-day time series with a duty cycle close to 100%. In the bottom panel, the PSD obtained after multiplying the same time series by a window mask corresponding to the Mark-I instrument –one of the BiSON helioseismic network (Chaplin et al. 1996) located at Observatorio del Teide– with a duty cycle of 23%. As expected, in the simulated ground-based data,

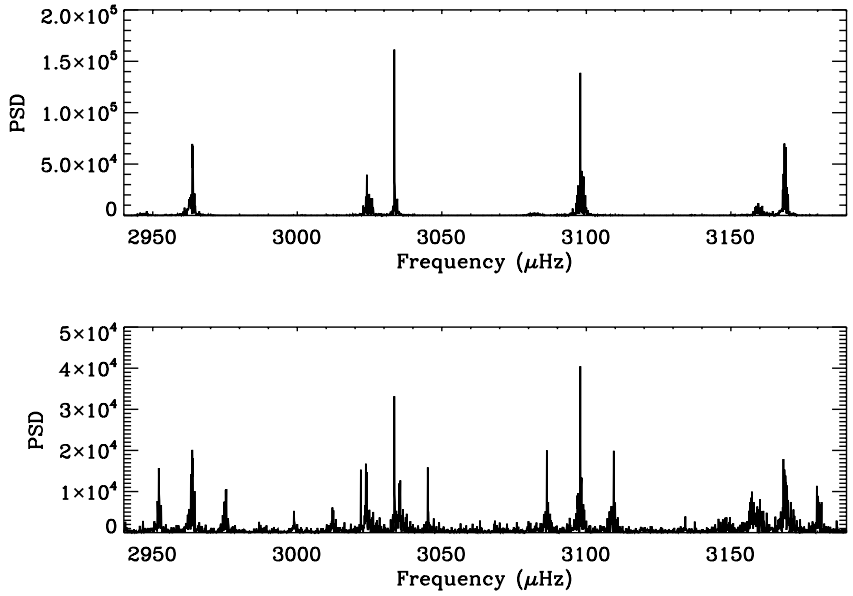

Fig. 22. Power spectrum density of 100 days helioseismic GOLF data with nearly 100% coverage (Top panel). The bottom panel represents the PSD of the same data but after multiplying by a realistic window function of 23% duty cycle obtained from the Observatorio del Teide.

every single solar mode is replicated at frequencies multiple of 11.57 μHz, complicating the analysis.

Regular short (typically one or two points) or longer gaps (up to a day or so) can be found in space missions such as CoRoT or *Kepler*. For example, the normal operations of this latter spacecraft involves the angular momentum dump of the reaction wheels every 3 days producing typical regular gaps of one long-cadence (29.42 min) or several short-cadence (58.85 s) measurements (Christiansen et al. 2013). Moreover, every month the satellite stops the scientific observations program to point towards the Earth and downlink all the data recorded on board. This interruption has a typical size of about a day (see for a detailed explanation of the *Kepler* gaps García et al. 2014b). In both cases the effects, if they are not corrected, are the addition of harmonics of the stellar signals at all frequencies multiple of $\sim 1/3$ and $\sim 1/30$ days respectively. An example of the *kepler* window function over a perfect 2 μHz sinusoid is shown in Fig. 23. The power of the wave leaks at higher frequencies at multiples of the inverse of the gap's frequencies (García et al. 2014b).

To solve the problem imposed by the regular gaps, several techniques have been used in asteroseismology. One widely used algorithm to study classical pulsators –where the modes are highly coherent– is CLEAN (Roberts et al. 1987; Foster 1995). It is based on an iterative procedure that searches for consecutive maxima in the power spectrum.

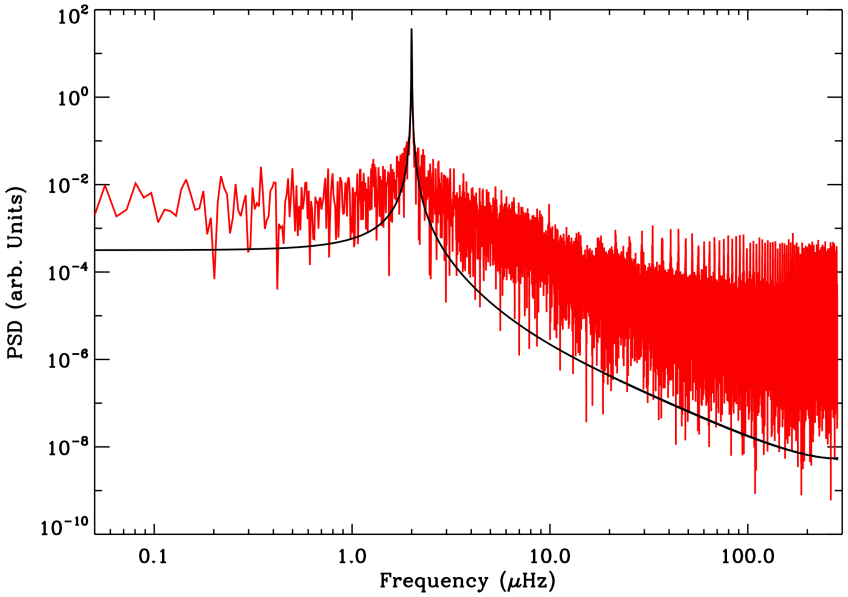

Fig. 23. Power spectrum density on logarithmic scale of a 2 μHz simulated sine wave (black) and after multiplying by the *Kepler* window function (red).

CLEAN starts by finding the highest peak in the periodogram, removing it in the time domain, recomputing the amplitude spectrum, and iterating for the next highest peak until a given amplitude threshold is reached. Some of the main caveats of the algorithm are that sometimes false peaks can be removed as being part of the signal, and any error on the properties of the retrieved peaks will introduce significant errors into the resulting cleaned periodogram. Finally, the use of this algorithm with stochastically excited modes is more complicated.

Another approach consists of interpolate the data in the gaps. Since the pioneer's work on helioseismology, several methods have been proposed to interpolate these datasets (e.g. Fahlman & Ulrych 1982; Brown & Christensen-Dalsgaard 1990). Although they work quite well, they require in general some a-priori knowledge of the signal to be treated. Although this worked well for the Sun because we know pretty well its main seismic properties, those algorithms are not well suited to treat thousands of unknown asteroseismic targets as it is the case on present and future space missions. Hence a simpler approach was first adopted by the CoRoT project consisting to perform linear interpolation (Auvergne et al. 2009; Samadi et al. 2007) on the main solar-like targets observed in the asteroseismic field (e.g. Appourchaux et al. 2008; **?**). However, in some cases a more refined interpolation algorithm was used in the analysis of these CoRoT data due to the limitations of the linear approach (e.g. Mosser et al. 2009b; Ballot et al. 2011).

Recently, an interpolation algorithm based on in-painted techniques (Pires et al. 2015) has been applied to asteroseismic data from CoRoT (e.g. Mathur et al. 2010a; Pires et al. 2015) and *Kepler*, providing very good results to minimize the impact of the multiples of the orbital frequency at 161.7 μHz and the gaps due to the perturbed data collected during the crossing of the South Atlantic Anomaly. An example of the application of these algorithm to the *Kepler* active F star KIC 3733735 (Mathur et al. 2014a) is shown in Fig. 24. Indeed, the final procedure to correct the CoRoT data will propose this interpolation.

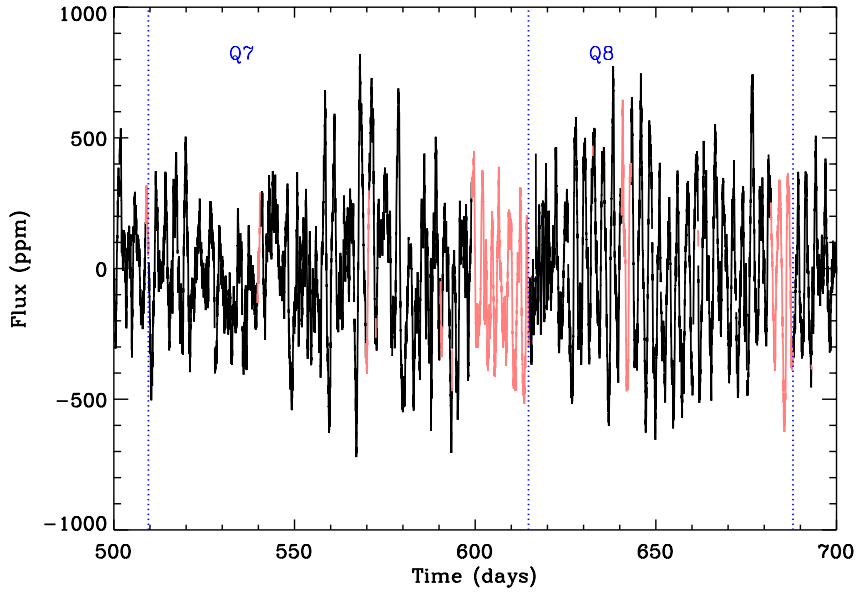

Fig. 24. Light curve of the *Kepler* F star KIC 3733735 taken during quarters 7 and 8 (black). The vertical blue dotted lines mark the separation between quarters. The pink segments of the light curves has been obtained by the inpainting interpolation.

Inpaint methods (Elad et al. 2005) are based on a prior of sparsity. In other words, the sparsity concept assumes that there is a representation of the signal in which most of the coefficients are close to zero. In the case of a single sine wave for example, the sparsest representation would be the Fourier transform because most of the Fourier coefficients would be zero except one (hence sparse), which is sufficient to represent the sine wave in the frequency space. Therefore in asteroseismology, and to deal with the large variation of gap sizes (from 1 short-cadence data point to ∼16 days), the best representation is the Discrete Cosine Transform (see for more details Pires et al. 2015, and references therein).

2.7 Precision and detectability of modes

To detect a mode in a periodogram it is required that the peaks rise above the general noise by a given factor, which can be translated into a minimum detection probability of 90%, or a more conservative value of 99% confidence level. In principle, the stellar background noise, which is the main source of noise in the frequency region where stochastically excited modes lie, cannot be reduced with a single set of observations. The situation is slightly better in helioseismology where stereoscopic observations of the Sun through two different viewing angles (e.g. STEREO mission, Kaiser et al. 2008) allows to simultaneously observe two non-coherent backgrounds. The other important sources of noise are the instrumental and statistical noise. Let's see other methods to compute the periodogram that can reduce the noise and enhance the signal-to-noise ratio of the observations.

Before that, it is important to say a word on the frequency precision that can be obtained. Libbrecht (1992) deduced an expression for the frequency precision that can be obtained in a typical seismic observation:

$$\sigma_\nu = \sqrt{f(\beta)\frac{\Gamma}{4\pi T}} \quad , \tag{2.23}$$

where $1/T$ is the frequency resolution, Γ is the line width of the modes, and β is the inverse of the SNR. $f(\beta)$ is given by the expression:

$$f(\beta) = \sqrt{1+\beta}\left[\sqrt{1+\beta} + \sqrt{\beta}\right]^3 \quad . \tag{2.24}$$

This expression, which is a generalization of the case without background (β=0, Duvall 1990), is only accurate when the observation time is much longer than the mode lifetime ($T >> \Gamma^{-1}$). It says that the mode precision is proportional to the square root of the mode linewidth and is proportional to the square root of the frequency resolution (for more details see, Appourchaux 2014).

The amplitude of stochastically excited modes in solar-like stars follows (Kjeldsen & Bedding 1995):

$$\frac{A}{A_\odot} \approx \frac{L}{M}\left(\frac{T_\odot}{T_{\rm eff}}\right)^s \quad , \tag{2.25}$$

where the exponent s is 0 for Doppler velocity measurements and $s = 2$ for photometric observations.

Assuming a Lorentzian profile for the modes, the maximum mode height in the power spectrum at $\nu_{\rm max}$ is directly related to the maximum mode amplitude and the mode lifetime as follows (Chaplin et al. 2009):

$$H = \frac{2A^2}{\pi\Gamma} \quad . \tag{2.26}$$

Therefore, we can derive a relation between the height, H and the frequency of maximum power, $\nu_{\rm max}$:

$$H = \frac{2A_\odot^2}{\pi\Gamma_{\rm max}}\left(\frac{T_{\rm eff}}{T_\odot}\right)^{7-2s}\left(\frac{\nu_\odot}{\nu_{\rm max}}\right)^2 \quad . \tag{2.27}$$

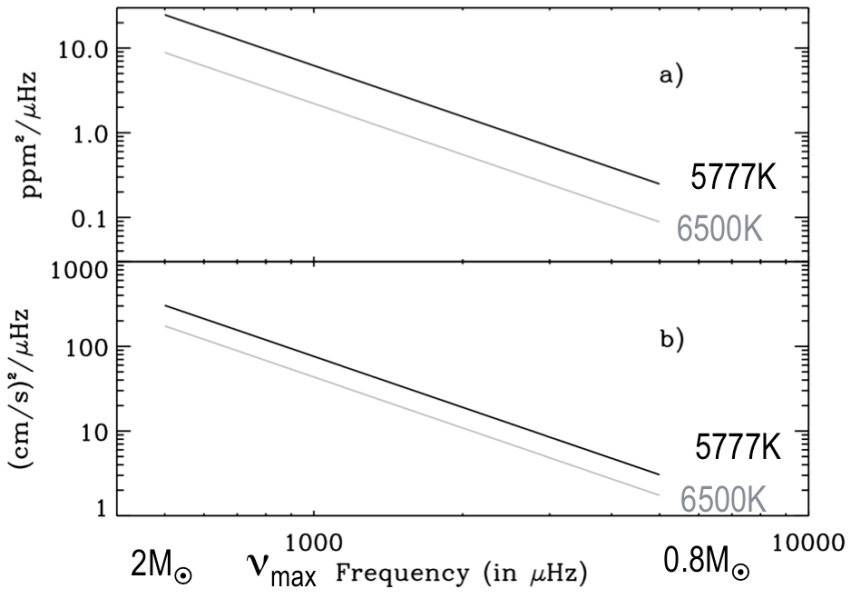

Fig. 25. Background noise as a function of $\nu_{\rm max}$ required to detect acoustic modes with a SNR of 10 for Doppler intensity (top) and velocity (bottom) observations and for two main-sequence stars, a cooler one (black) with $T_{\rm eff}$ = 5777K (mode line widths of 1 μHz and a hotter F star (grey) with $T_{\rm eff}$ = 6500K and a mode line width of 4 μHz. Adapted from (Appourchaux & Grundahl 2015).

It is important to note that the CoRoT and *Kepler* observations seem to show that there is a relation between the line width of the modes and the effective temperature of the star (Baudin et al. 2011; Appourchaux et al. 2012a; Corsaro et al. 2015).

It is represented in Fig. 25 the background noise as a function of $\nu_{\rm max}$ required to detect acoustic modes with a SNR of 10 for Doppler velocity and intensity observations and for two main-sequence stars, a cooler one with $T_{\rm eff}$ = 5777K (mode line widths of 1 μHz) and a hot F star with $T_{\rm eff}$ = 6500K and a mode line width of 4 μHz (see for more details the discussion in Appourchaux & Grundahl 2015).

2.8 Other Periodogram estimators

In the previous sections we have described the two most common ways to compute a periodogram in asteroseismology: the FFT when we have to deal with evenly distributed time series, and the Lomb-Scargle periodogram for irregularly sampled time series. In the rest of the section other ways to compute the periodogram will be described. These methods (or variations of the previous ones) have the advantage that they can increase the SNR of the signals in some particular circumstances. Indeed, the Fourier spectrum is very well adapted to periodic functions.

2.8.1 Average Power Spectrum

Sometimes, it can be useful to split the observations into several smaller chunks of data and average the independent spectra, instead of doing one single periodogram corresponding to the full time series. Thus, the average Power Spectrum (AvPS) of N independent time series can be calculated as:

$$AvPS = \sum_{i=1}^{N} \mid F_i(\nu) \mid^2 \quad . \tag{2.28}$$

The AvPS has the advantage of reducing the variance of the incoherent noise and improving the statistics. This periodogram can also be applied when two observations are separated by a long gap. This was the case of the CoRoT observations of HD 49933 in which the two first observing runs were separated by $\sim$ 1 year (Benomar et al. 2009b). In such case, it is more convenient to compute the average of the two independent observations than computing the full periodogram with a 1 year gap in between. It is important to note that the AvPS has a reduced frequency resolution (corresponding to the size of the individual chunks of data) and thus, it can only be used when the resolution is enough for the problem we want to study.

It can be demonstrated (Appourchaux 2003) that the statistics of the AvPS of independent time series follows a χ^2 with $2N$ degrees of freedom. As a practical recipe, the AvPS can be fitted with a standard maximum likelihood estimator and the error bars can be normalized by $\sqrt{N}$ (Appourchaux 2003).

2.8.2 Multitaper spectral analysis

Multitaper Spectral Analysis (MTSA) methods consist of multiplying a single light curve by a series of functions (windows) called tapers. MTSA methods are an extension of single-taper spectral analysis where the time series are multiplied or apodized by a single window function such as a Hanning window. This taper gives less weight to the ends of the time series than to the center, reducing the effect of the squared window (the Sinc function in Eq. 2.14) in the periodogram (Thomson 1982). The multitaper approach uses a variety of orthogonal tapers, some of which give more weight to the ends of the time series and others to the center, with a good compromise between any biases and the reduction of the global variance (Percival & Walden 1993).

In practice MTSA analysis involves the calculation of the windowed functions $f_k(t) = f(t)h_k(t)$, where $f(t)$ is the time series and $h_k(t)$ represents the k taper. Thus the Multi Taper (MT) spectrum is the average of the power spectrum of the individual windowed functions:

$$MT \text{ Spectrum} = \sum_{k=1}^{N} \mid \overline{f_k(t)} \mid^2 \quad . \tag{2.29}$$

The statistics of the MT spectrum built in such ways are a χ^2 with $2N$ degrees of freedom (Thomson 1982). It can also be demonstrated that the variance of the MT spectrum is reduced by a factor $\sim 1/N^3$ (Komm et al. 1999).

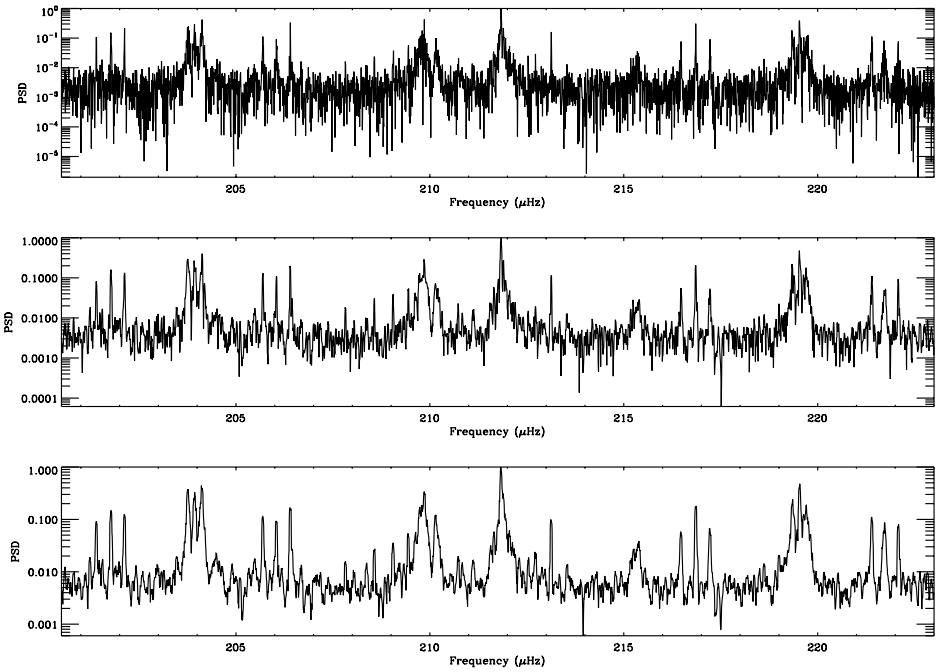

Fig. 26. Comparison between the Lomb-Sargle periodogram (top) represented in log scale and a MT spectrum computed with 3 (middle) and 6 (bottom) sinusoidal tapers for the *Kepler* target KIC 5356201.

Several functions can be used as tapers (e.g. Slepian tapers, Slepian 1978), but they are difficult to calculate. Indeed a simpler approach is to use as tapers sinusoidal functions in which the first taper is similar to a Hanning window (Komm et al. 1999). In Fig. 26 we compare a Lomb-Scargle spectrum with a MT spectrum computed with 3 (middle) and 6 (bottom) sinusoidal tapers. The higher the order of the taper, the smaller the variance of the spectrum. However, the MT spectrum tends to enlarge the width of the modes. Therefore the number of tapers that can be used would be limited by the lifetimes of the modes we want to measure.

2.8.3 Average Cross Spectrum: Temporal and Spatial

The observation of the same physical phenomena with two independent measurements provide a reduction of noise by a factor $\sqrt{2}$ in amplitude (2 in power). Using cross-correlation techniques we can define the averaged cross-spectrum (AvCS) as the average of the complex product of the Fourier transform of one data set, $A(\nu)$, by the complex conjugate of the Fourier transform of another, $B(\nu)$ (Elsworth et al. 1994; García et al.

1998a):

$$AvCS = \frac{1}{N}\sum_{k=1}^{N} A_k(\nu)B_k^*(\nu) \tag{2.30}$$

The significance of the AvCS can be computed from the coherency:

$$\text{Coherency}(\nu) = \frac{\sum_{k=1}^{N} A_k(\nu)B_k^*(\nu)}{\sqrt{\sum_{k=1}^{N} A_k(\nu)A_k^*(\nu)\sum_{k=1}^{N} B_k(\nu)B_k^*(\nu)}} \tag{2.31}$$

Appourchaux et al. (2007) demonstrated that the mean of the AvCS tends to zero for independent series (instead of to a value of $2\sigma^2$ for standard averaged power spectra) while the sigma remains the same compared to the standard averaging of the power spectrum of independent series. Therefore, the average level in the AvCS is reduced compared to the mean spectrum while the dispersion stays the same. This implies that the SNR of resolved peaks will increase. This methodology was successfully applied to 157 four-day time series of the two independent channels of the GOLF instrument (properly calibrated in velocity following García et al. 2005) in order to reduce the photon noise at high frequency (see Fig. 27). This allowed to uncover the existence of high-frequency peaks in Sun-as-a-star observations (García et al. 1998a).

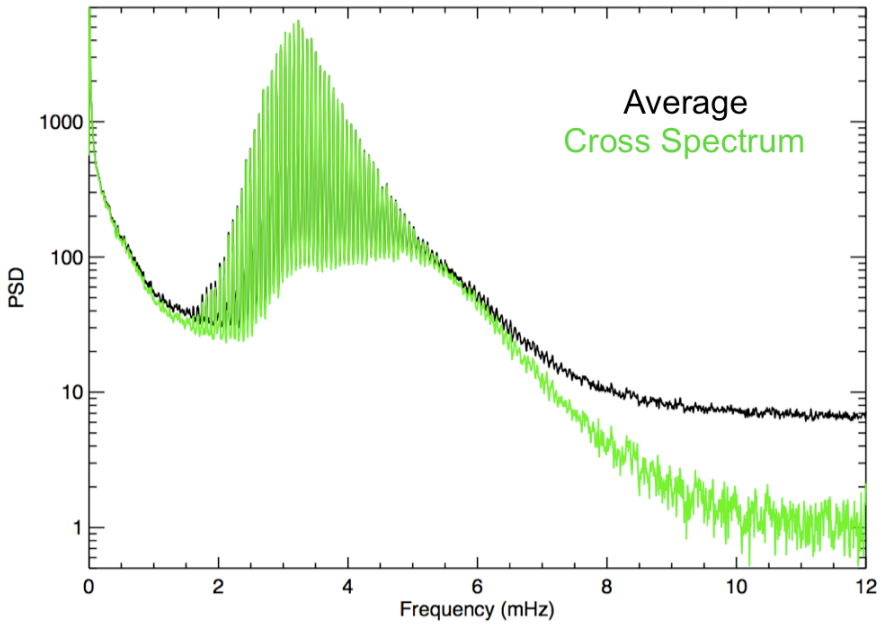

Fig. 27. Comparison between the AvCS (in green) and the standard average (black) of 157 subseries of 4 days smoothed by a 5 points boxcar function.

Unfortunately, we do not always have two simultaneous and independent measurements of the same physical phenomenon. Alternatively, when we are not interested in the high-frequency part of the spectrum (above $\nu_{\rm Nyq}/2$), García et al. (1999b) demonstrated that we can built two independent time series by splitting the original time series in two, one containing the odd measurements and the other, the even points. The Interleave-shift Cross Spectrum (ISCS) is then the AvCS where the two independent series are the two that were just built. Because there is a small time delay between the two time series, it was proposed to shift the phases of the second channel by the sampling time. By construction, the new time series have a sampling rate doubled, which implies that $\nu_{\rm Nyq}$ of the ISCS is reduced to half.

The same procedure could be applied in the space instead of the temporal domain to imaged helioseismic instruments such as SoHO/MDI or SDO/HMI in order to reduce the convective background (for more details on this procedure see García et al. 2009). In this case, the granulation noise has a small correlation from one pixel to the next and the overall background level is reduced.

3 Preparing the time series

Any seismic analysis starts by collecting time series of a given phenomenon, e.g., the photometric variation of the flux of a star or the Doppler velocity displacement of the spectral lines formed in the photosphere of the Sun or other stars. Unfortunatelly, in many cases, the time series obtained from the observations are not directly exploitable and some preparation is needed. This involves correction from any known instrumental drifts and perturbations occurred during the observations, the inter-calibration of the observations taken by different instruments (for example when a network of ground-based telescopes is used), etc. Due to the nature of the seismic analyses, special care is always required in the handling of the timing of every measurement. All the subsequent analyses done from the time series rely on an accurate timing of the data points.

Although the calibration of any time series is completely dependent on the instrument(s) that collected the data and the scientific objective of the analysis, there are several common steps that we are going to summarize in the following section based on the calibration procedure of the *Kepler* data for seismic analysis including the surface dynamics, which means keeping the stellar signal at low frequencies. A more detailed description can be found for example in García et al. (2011), Thompson et al. (2013), and Handberg & Lund (2014).

Kepler is located in a 372.5-day, Earth-trailing, heliocentric orbit. This requires to perform 90° rolls about its axis every 93 days to maintain the solar panels illuminated and the radiator, which cools the focal-plane arrays, pointed away from the Sun (Haas et al. 2010). Data are consequently subdivided into quarters (denoted Qn or Qn.m, where n is the quarter number and m, the month), starting with the initial 10 days commissioning run (Q0), followed by a 34 days long first quarter (Q1) and subsequent three months quarters (Q2, Q3,...), up to the last observations during Q17.

For each star, two types of observations are available: ‘The pixel-data files” and the integrated light curves. In both cases they are corrected for some instrumental effects, although not all. The pixel-data files are CCD stamps (also known as “imagettes in the

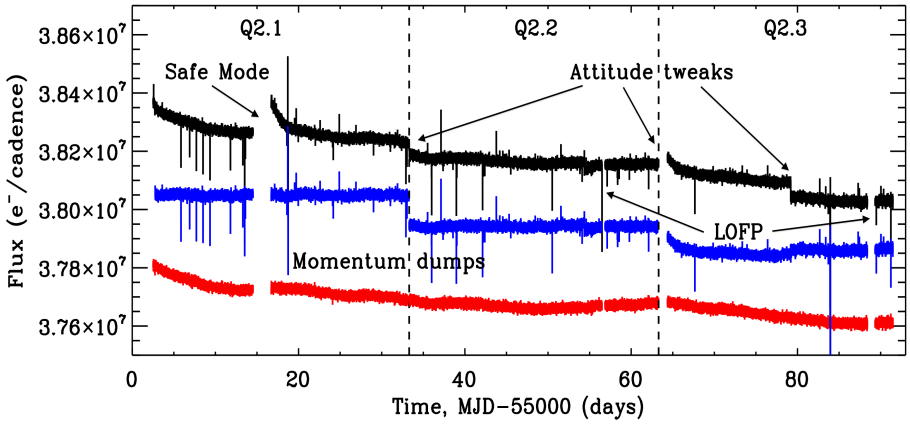

Fig. 28. Raw (black), PDC corrected (blue) and corrected –using the procedure described in this paper (red)– light curves of the solar-like target: KIC 11395018 (Mathur et al. in preparation). The corrected light curve has been shifted down, by 4 10^5 e^-/cadence, for the clarity of the comparison. The origin of the time axis is in Modified Julian dates (MJD) - 55000. The points in which the flux fall down are most of them due to momentum-dump operations. LOFP stands for: Loss Of Fine Pointing. Image from García et al. (2011).

CoRoT community) centered at each star and covering all the pixels that contains signal from the star. They allow individual scientist to perform their own aperture photometry following their own requirements. The integrated light curves are part of the products provided by NASA from the Pre-Data-Conditioning (PDC) allowing to search for exoplanet transits (Jenkins et al. 2010).

While these PDC datasets, either the PDC-SAP (Simple Aperture Photometry) or the PDC-msMAP (multi scale Maximum A Posteriori methods) are in constant evolution and new and more refined procedures are established, part of the low-frequency stellar signal (such as the one produced by starspots or low-frequency modes) could be filtered. Therefore, for solar-like oscillating stars as well as some classical pulsators (δ-Scuti and Γ-Doradus stars), it is better to take the pixel-data files and develop a specific set of corrections that takes into account the particularities of the oscillating signal that we are interested in.

In general, light curves should be corrected for three types of instrumental effects (see Fig 28): outliers, jumps, and drifts. Outliers are those measurements showing a too large point-to-point deviation. Following the procedures described by García et al. (2011) that are based on the ones developed for GOLF/SoHO (García et al. 2005). The deviation is computed on the backward difference function of the light curve (García & Ballot 2008) with a threshold greater than 3σ, where σ is defined as the standard deviation of the backward difference of the time series. This correction removes $\sim 1\%$ of the data points.

Jumps are defined as sudden changes in the mean value of the light curve due, for example, to attitude adjustments or because of a sudden pixel sensitivity drop. Finally, drifts are small low-frequency perturbations, which are in general due to temperature

changes (after, for example, a long safe mode event) that last for a few days and are corrected using polynomial fits.

Once these corrections are applied, we build a single time series after equalizing the average counting-rate level between all the quarters (red curve in Fig. 28). A change of the average counting rate can also happen inside a roll when the aperture mask is changed. To do this equalization and to convert into parts per million (ppm) units, we use a low-pass filter of the data. The details on the filter and its cutoff frequency depends on every calibration procedure.

The light curves from CoRoT or *Kepler* suffer from some discontinuities. As seen in Sect. 2.6 those gaps are usually interpolated.

4 The observed stellar power spectrum

The natural way to study stellar oscillations is by analyzing the Fourier components of the signal. In the analysis of solar like stars, it is common to ignore the phase information and work with the power spectrum, or the power spectrum density (PSD).

4.1 Generalities

The PSD of the *Kepler* target KIC 3733735 is shown in Fig. 29. This star is a typical hot F main-sequence solar-like star. Depending on the frequency range, the spectrum is dominated by the features related with a different physical phenomena.

Starting by the low-frequencies (between 1 and 10 μHz), the spectrum is dominated by a series of high-amplitude peaks and their harmonics. This is the signature of the surface differential rotation of the star through the modulation induced by the stellar spots crossing the visible stellar disk. The surface differential rotation of this star exhibits two active bands, one spinning at $\sim$ 3 days and another one at $\sim$ 2.5 days (Mathur et al. 2014a; García et al. 2014a). At higher frequencies, between 50 and 1000 μHz, the spectrum is dominated by convection (granulation). At even higher frequencies, it is possible to distinguish the bump of the acoustic modes centered at around 2000 μHz. Finally, close to the Nyquist frequency, the spectrum is flat and it is dominated by the photon noise of the instrument.

4.2 Global oscillation parameters: $\Delta\nu$ and $\nu_{\rm max}$

As seen in Fig. 29, when the SNR is enough (e.g. Chaplin et al. 2011b), the power spectrum of any solar-like star shows a power bump in which a repetitive structure or pattern of modes is visible (see Fig. 30 for the *Kepler* star 16 Cyg A). The power bump allows the definition of the frequency of maximum power, $\nu_{\rm max}$, which is related with the acoustic cutoff frequency (Brown et al. 1991; Kjeldsen & Bedding 1995; Belkacem et al. 2011, 2013). To measure $\nu_{\rm max}$, it is common practice to fit a Gaussian function within the convective background fit (see for more details Sect. 5.3).

Looking in more details to the p-mode bump, it is composed by a repetitive sequence of odd and even degree modes. Thus, two important seismic variables can be defined: the large- and the small-frequency separations or simply large and small separations.

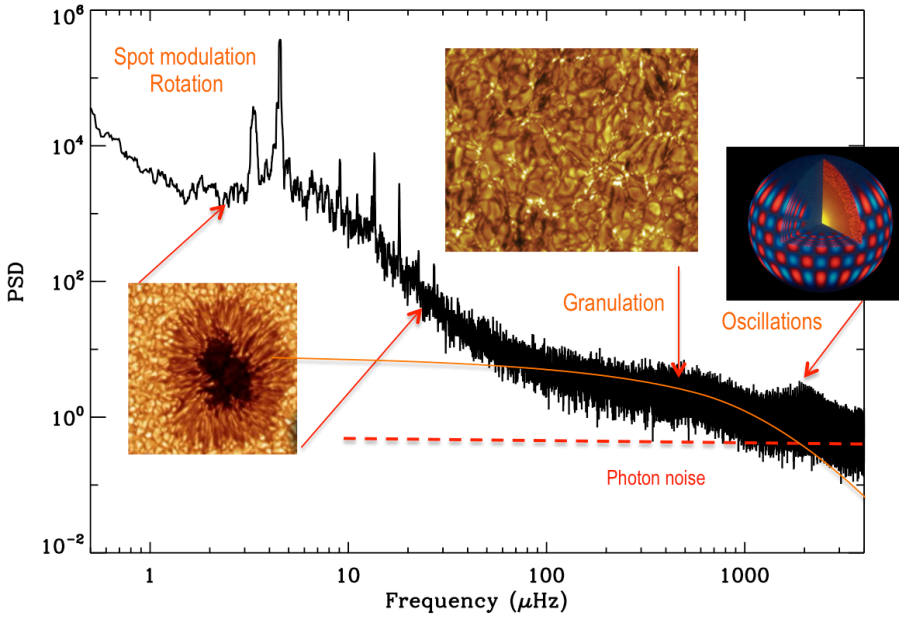

Fig. 29. PSD of the *Kepler* target KIC 3733735 observed in short cadence during three years. Physical phenomena associated with each region of the PSD are indicated: photon noise, oscillations, convection (granulation), and rotation through the spot modulation of the emited stellar flux.

The large separation of low-degree p modes is given by (see also Fig. 30):

$$\Delta\nu_\ell(n) = \nu_{n,\ell} - \nu_{n-1,\ell} \quad . \tag{4.1}$$

This large separation depends inversely on the sound-travel time between the center and the surface of the star (see e.g. Christensen-Dalsgaard 2002a) which means, it is proportional to the square root of the mean density in the cavity in which the modes propagate:

$$\Delta\nu_\ell(n) = \left[2\int_0^R \frac{dr}{c_s}\right]^{-1} \quad , \tag{4.2}$$

where R is the stellar radius, and c_s is the sound speed. In the case of the Sun, the mean large separation has a value of ~135 μHz.

The small separation of low-degree p modes is given by (see also Fig. 30):

$$\delta\nu_{\ell,\ell+2}(n) = \nu_{n,\ell} - \nu_{n-1,\ell+2} \quad . \tag{4.3}$$

This difference is mainly dominated by the sound-speed gradient near the core and, therefore, it is sensitive to the chemical composition in the central regions. Indeed, the small separation is the difference of two modes with nearly identical eigenfunctions in the

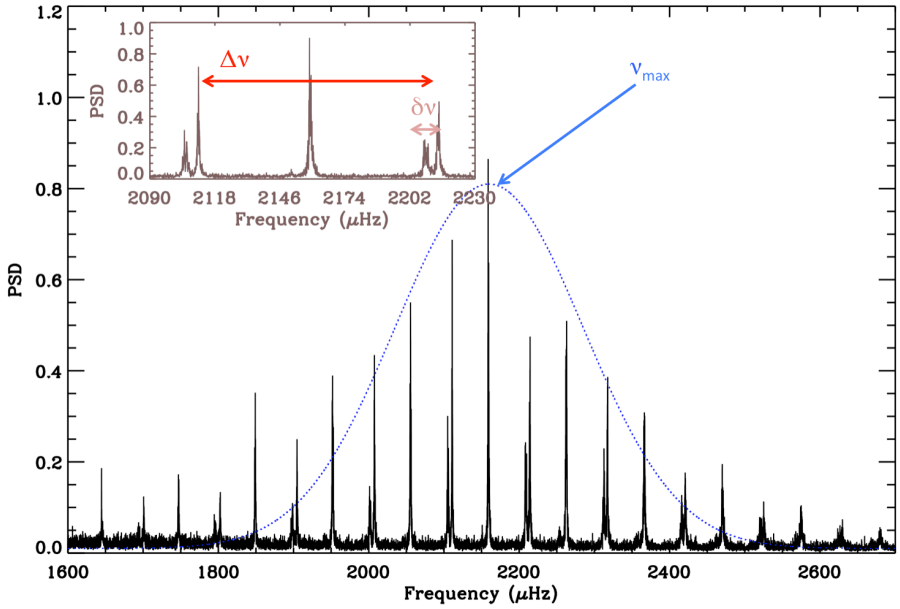

Fig. 30. PSD (in arbitrary units) of the *Kepler* target 16 Cyg A. The blue doted line represents the Gaussian fit to obtain the frequency at maximum power, $\nu_{\rm max}$. The inset is a zoom showing the large frequency separation, $\Delta\nu$, between two modes ℓ=0 and the small separation $\delta\nu_{0,2}$

surface (similar outer turning points) and being only different in the deeper layers, with different inner turning points (see right panel in Fig. 2). It is important to notice that we can also define another small separation between the radial and the dipole modes. In this case we define $\delta_{0,1}$ to be the amount by which the modes ℓ=1 are offset from the midpoint of the modes ℓ=0 on either side:

$$\delta\nu_{0,1}(n) = \frac{1}{2}(\nu_{n,0} + \nu_{n+1,0}) - \nu_{n,1} \quad . \tag{4.4}$$

Using the asymptotic theory it can be shown that (Christensen-Dalsgaard & Berthomieu 1991):

$$\delta\nu_{\ell,\ell+2}(n) \simeq -(4\ell+6)\frac{\Delta\nu_\ell(n)}{4\pi^2\nu_{n,\ell}}\int_0^R \frac{dc_s}{dr}\frac{dr}{r} \quad . \tag{4.5}$$

As the frequencies of both modes are very close, they have similar near-surface effects and the small separation is less affected by such effects. However, some residuals can still remain and therefore, it has been demonstrated that the ratio of the small separation to the large separation, defined as $r_{0,2} \equiv r_{0,2}(n) = \delta\nu_{0,2}(n)/\Delta\nu_\ell(n)$, can exclude such effects to a great extent (see for more details Roxburgh & Vorontsov 2003).

Although the oscillation spectrum is not perfectly regular and they slightly vary with frequency, it is possible to use this regularity to look for the large period spacing. Either by computing the power spectrum of the power spectrum (e.g. Hekker et al. 2010; Huber et al. 2009; Mathur et al. 2010b) or by computing the autocorrelation of the signal (e.g. Roxburgh & Vorontsov 2007; Mosser & Appourchaux 2009), it is possible to determine the large (and the small) frequency separations in a global way. Another way consists on fitting a few modes around $\nu_{\rm max}$ and extract in such way the large frequency spacings as well as other global parameters as the phase shift term ϵ (Kallinger et al. 2012). We will describe in more details the fitting techniques in the next section of this chapter.

It is important to notice that the global techniques does not normally extract the large spacing but half of it because the main periodicity retrieved is the distance between the odd and the even modes. However, there is a family of evolved stars called: "depressed dipole mode stars" (García et al. 2014c; Mosser et al. 2012a), in which the $\ell = 1$ modes have lower-than-expected amplitudes and thus the value retrieved by the automatic pipelines is directly the large separation.

4.3 The échelle diagram

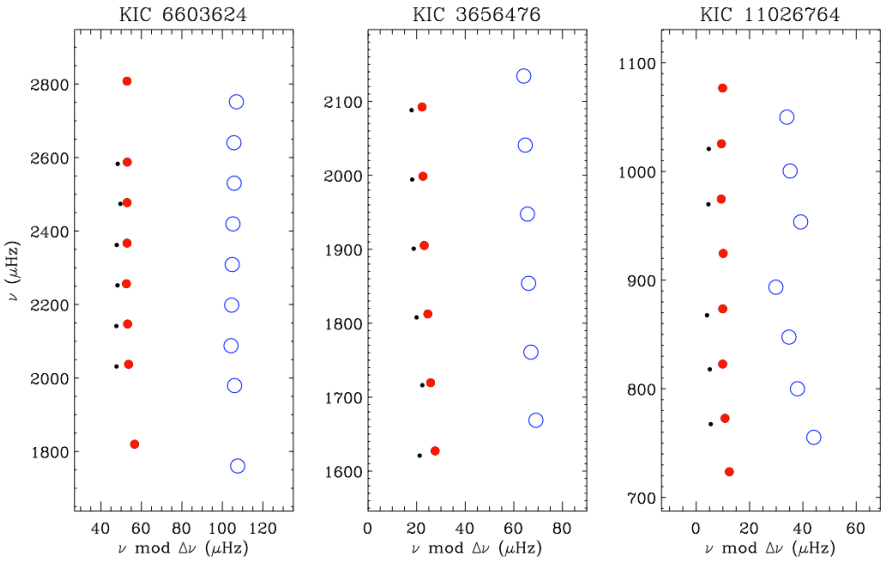

Fig. 31. Échelle diagrams of 3 solar-like stars observed by *Kepler*, showing the $\ell = 0$ (filled red symbols), $\ell = 1$ (open blue symbols), and $\ell = 2$ (small black symbols) ridges. Extracted from Chaplin et al. (2010).

The échelle diagram is a 2-D representation of the power spectrum in which the frequency is plotted as a function of the frequency modulo the large frequency separation.

In other words, it is build by cutting the spectrum in segments of multiples of the large-frequency spacing and stacking them one in top of the next. In such way, modes that are equally spaced by this quantity are aligned forming vertical ridges. It was originally introduced in helioseismology by Grec et al. (1980) to correctly identify the modes of the power spectrum of the Sun measured from the South Pole. Nowadays, this type of diagram is commonly used in asteroseismology to properly tag the degree and the order of the modes. Moreover, any departures from regularity is clearly visible as a curvature in the individual ridges of each mode degree. For example, variations in the small separations appear as a convergence or divergence of the corresponding ridges. It is very useful to identify bumped modes (those displaced from its original position due to the presence of a mixed mode in the vicinity) as well as the presence of mixed modes. In Fig. 31 the échelle diagram of 3 solar-like stars observed by *Kepler* is shown. The ridges corresponding to the even modes are clearly shown on the left-hand side of the diagrams, while the ridge of the ℓ=1 is visible onto the right. Because the amplitude of the ℓ=3 modes is very small the odd ridge is composed of only one set of modes in most of the stellar observations. From left to right, stars are more and more evolved. Indeed the Échelle digram of KIC 11026764 (right-hand side panel) shows a bumped ℓ=1 mode (a mode that have been moved from its original position by the presence of a mixed mode or by the mode immediately below) at $\sim$ 900 μHz. This is a clear signature that this star is a sub-giant star. This kind of diagrams clearly help in the identification of the modes.

5 Characterizing the p-mode spectrum

In this section we describe the methodology to characterize the acoustic modes over the entire p-mode range in both, Doppler velocity and luminosity observations. We will explain the main difference between the solar and the stellar case, as well as the difference when dealing with sub giants and giants in which the apparition of mixed modes complicates the analysis.

To extract the properties of the modes it is necessary to fit a given model to the data, while providing statistical tools for *hypothesis testing* and take a decision on whether or not the model and/or the hypothesis is accepter or rejected. To reach this goal, there are two different approaches, the *frequentist* and the *Bayesian*. In the frequentists approach, the laws of physics are deterministic and future realizations of an event are conditioned by past realizations. If the result of an experiment or event has occurred 20% of the times, a new realization of the same event will have this probability that the solution would be the same. In the Bayesian approach (Bayes 1763), each realization will be conditioned by other considerations that could change the probability attributed to this particular realization, i.e., there is an a-posteriori evaluation of the chances of each possible result.

In this course we will not go further in the discussion between this two statistical approaches and we will only provide the general framework of how to model the stellar spectra and the general steps that are required to fit the spectrum. An example will be given following the frequentist approach. I recommend the reader the excellent review by Appourchaux (2014) to uncover the details of both statistical approaches.

5.1 Modeling the acoustic spectrum

A useful analogy for the stellar acoustic modes is that of an ensemble of harmonic oscillators, excited stochastically, and damped intrinsically by turbulence in the outer layers of the convection zone (e.g. Goldreich & Keeley 1977; Goldreich & Kumar 1988). Each resonant component can be represented in the form:

$$\frac{d^2x(t)}{dt} + 2\eta\frac{dx(t)}{dt} + (2\pi\nu_o)^2 x(t) = f(t) \tag{5.1}$$

where $x(t)$ is the displacement of the oscillator, η its damping rate, ν_o the frequency of the undamped oscillator and $f(t)$ the random forcing function. The Fourier transform of the oscillator equation gives a Lorentzian shape for the expected power spectrum of the signal in the vicinity of the resonance, under the assumption that $F(\nu)$ – the power spectrum of $f(t)$ – is a slowly-varying function of ν, and $\eta \ll \nu_o$. The maximum height (power density) of the resonant peak in the frequency domain is then given by:

$$H = \frac{F(\nu)}{16\pi{\nu_o}^2\eta^2}, \tag{5.2}$$

and its width at half-height by:

$$\Gamma = \frac{\eta}{\pi}. \tag{5.3}$$

Even though the solar low-ℓ mode peaks exhibit small amounts of asymmetry—typically of the order of a few percent (e.g. Nigam & Kosovichev 1998; Toutain et al. 1998; Chaplin et al. 1999b; Thiery et al. 2000)—the magnitude of this is so small that for the moment we will assume that a Lorentzian description is sufficiently accurate for our purposes here. Indeed it is usually neglected in asteroseismic analyses. The integrated power[2], P, of a single mode is then given by:

$$P = \frac{\pi}{2}H\Gamma. \tag{5.4}$$

The total energy in the mode, E, is taken to be the sum of the kinetic and potential energy and can be written as:

$$E = \mathcal{I}P, \tag{5.5}$$

where $\mathcal{I}$ is the corresponding mode inertia. Since we will ignore possible changes in $\mathcal{I}$, variations in P and E are identical. The rate at which energy is dissipated in the modes (also sometimes referred to as the acoustic noise generation rate, e.g., Houdek et al. 1999) can be derived by using the analogy of the harmonic damped oscillator (e.g. Chaplin et al. 2000):

$$\frac{dE}{dt} = \dot{E} = 2\pi H\Gamma^2. \tag{5.6}$$

From the above equations, we should expect: the linewidth to provide a direct measure of the damping rate; the mode power (or mode energy) to provide a measure of the balance between the excitation and damping of the modes; and the energy supply rate to provide a diagnostic of the forcing or excitation.

[2]For Doppler velocity observations, this will correspond to the integrated velocity power; while for photometric observations this will provide a measure of the total power in the intensity fluctuations associated with the mode.

5.2 Extraction of mode parameters

5.2.1 Helioseismology

The close proximity of modes in the power spectrum of each time series demanded that the low-p modes be fitted in pairs (i.e., monopole modes with quadrupole modes, and dipole modes with octupole modes, see an example in Fig. 32) to avoid any bias in the extraction of the mode parameters due to their proximity in frequency. We modeled the power in each modal component of radial order n and angular degree ℓ with azimuthal order m with an asymmetric Lorentzian profile (Nigam & Kosovichev 1998), as:

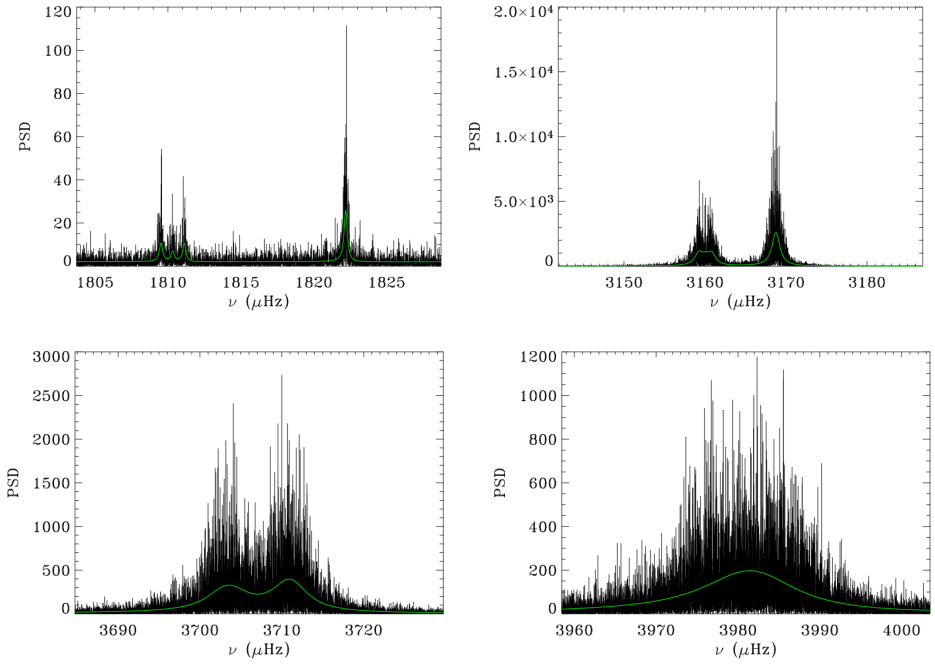

Fig. 32. Example of fits (green line) ℓ=2, 0 and ℓ=3, 1 modes, left- and right-hand side panels respectively at low (top) and high (bottom) frequencies of a typical GOLF spectrum. In the first case, the lifetimes of the modes are longer and therefore the linewidths are smaller than for the modes at high frequency.

$$P(x) = H\frac{(1+bx)^2+b^2}{1+x^2} \tag{5.7}$$

where $x = 2(\nu - \nu_o)/\Gamma$. H is the maximum power spectral density (often called the mode "height"), and the parameter b provides a measure of the fractional asymmetry of the

peak. The mode-pair model, M, to be fitted is then described in full by:

$$M(x,\vec{a}) = \sum_{m=-\ell,\ell} \beta^{\ell}_{|m|} P(x)_{n,\ell} + \sum_{m=-\ell,\ell} \beta^{\ell+2}_{|m|} P(x)_{n-1,\ell+2} + N, \tag{5.8}$$

where: $\vec{a}$ is the vector of parameters to be fitted; $\beta^{\ell}_{|m|}$ are the m-component height ratios in each multiplet; and N is the uncorrelated background (assumed to be constant across the frequency range defining the window of the fit).

Since the observed power is distributed about the limit spectrum with χ^2 2-d.o.f. statistics (e.g. Appourchaux et al. 1998), the probability (likelihood) function that must be maximized in the frequenctist approach (to give the model that makes the data most likely) takes the form:

$$f(X,\vec{a}) = \prod_{i=1}^{n} \frac{1}{M(x_i,\vec{a})} \exp\left[-\frac{X(x_i)}{M(x_i,\vec{a})}\right]. \tag{5.9}$$

One seeks to find the vector of model parameters $\vec{a}$ that maximizes $f(X,\vec{a})$ across the n frequency bins in the fitting interval. In practice we used a modified Newton method (Press et al. 1992) to minimize the negative logarithm of the likelihood function. The covariance matrix of the vector $\vec{a}$ is well approximated by the inverse of the Hessian matrix. The uncertainties on each fitted parameter are therefore taken as the square roots of the diagonal elements of the inverted matrix.

We imposed the following constraints when fitting each mode pair in order to reduce the number of free parameters and stabilize the peak-fitting procedure:

1. All components within a given multiplet (i.e., for a given ℓ) were assumed to have the same linewidth

2. A single height – that of the outer, sectoral components – was fitted for each mode. The relative m-component height ratios, $\beta^{\ell}_{|m|}$, were assumed to take fixed theoretical values as calculated, a priori, for each instrument (see a complete discussion on this point in Salabert et al. 2011a)

3. The components of both multiplets in a pair were assumed to possess the same peak asymmetry.

4. The natural logarithm of the height, width and background terms were varied—not the straightforward parameters themselves—in order to give a quasi-normal fitting distribution.

5. Prior to fit each pair of modes, we first compute the background parameters and we either divide the PSD by the fitted background model or we fix it in the fitting of the modes. See Section 5.3 for further details.

It is important to notice, that sometimes, we let all the parameters free for each mode or just a combination of them.

We also found that the size of the fitting window had important implications for the extracted asymmetry parameter. This was largely a result of the influence of neighboring $\ell = 4$ and 5 modes (a long discussion on this bias can be found in Chaplin et al. 2006). While these higher ℓ values are much less prominent in the Sun- as-a-star data than their fitted $\ell \leq 3$ counterparts, they nevertheless appear at sufficient amplitude to (subtly) affect parameter extraction. This is because the fitting models do not usually account for the presence of "leakage" from $\ell = 4$ and 5 into the fitting window (as we also omitted to do it here), although they can be measured in, for example, Sun-as-a-star observations using 12 years of VIRGO/SPM data (e.g. Lund et al. 2014).

5.2.2 Asteroseismology

In opposition to the "local fitting scheme" traditionally used in helioseismology in which narrow frequency bands are fitted, it has been proved that a global approach is better suited in the case of asteroseismology (e.g. Appourchaux et al. 2008, 2012b; Barban et al. 2009; Benomar et al. 2009b; Deheuvels et al. 2010; Mathur et al. 2011a, 2012).

Although fitting low-degree p-mode profiles in helioseismology and asteroseismology might appear very similar, the unknown stellar inclination angle makes the fitting of asteroseismic data much more difficult (see for example Appourchaux et al. (2008) for the case of the star HD 49933, Davies et al. (2014) for the case of the Sun, and Gizon & Solanki (2003) for Monte-Carlo simulations with artificial p-mode profiles). It is not only the lower signal-to-noise ratio of the p-mode asteroseismic signal that makes the fitting difficult, but also the high correlation between the inclination and the rotational splitting (Ballot et al. 2006, 2008). Because of that, the determination of these two parameters can be rather poor and will consequently affect the determination of the other parameters (frequencies, widths, heights, etc). Therefore, instead of fitting each multiplet or pair of modes individually – as commonly done in helioseismology – we chose to perform a global fitting of all the multiplets above a given amplitude threshold around the maximum of the p-mode hump, assuming that the rotational splitting is independent of the frequency (see Appourchaux et al. 2008, for all the details). This type of global method was pioneered by Roca Cortés et al. (1999) using solar data. By doing so, the splitting and the inclination angle are better constrained, even though the stars are then modeled as a rigidly rotating star. This condition can then be relaxed to allow fitting individual splittings for each mode while fixing the inclination angle (e.g. Beck et al. 2012; Deheuvels et al. 2012, 2014).

Each multiplet is described by five parameters: the central frequencies of the modes $\ell = 0, 1, 2$, one line width (the same for all modes within a large separation), and one mode height. In general, the same visibility ratio between angular degrees is assumed (Salabert et al. 2011a), unless there are indications that this relation does not hold (e.g. in the case of depressed dipolar mode stars, García et al. 2014c). An example of such global fit can be seen in Fig. 33 corresponding to the analysis of 11 orders of the CoRoT star HD 169392 (Mathur et al. 2013a).

It is important to note that in the solar case the variation induced in the p-mode parameters by magnetic activity (e.g, frequency shifts of the modes, amplitude modulation, etc) can be measured at different time scales (e.g. Woodard & Noyes 1985; Anguera Gubau

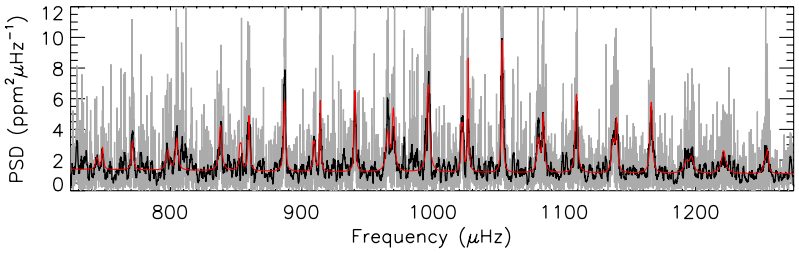

Fig. 33. Power spectral density (PSD) of HD 169392 in the p-mode region at full resolution (grey) and smoothed over 15 bins wide boxcar (black). The red line corresponds to the global fitting performed over 11 orders.

et al. 1992; Chaplin et al. 2001; Salabert et al. 2009; Fletcher et al. 2010; Salabert et al. 2015; Howe et al. 2015). In ateroseismology, these magnetic effects are not taken into account yet, although they can be measured in some targets (e.g. García et al. 2010; Salabert et al. 2011b). The good news is that magnetic activity seems to inhibit stellar pulsations and thus, the solar-like pulsating stars are those with the weakest magnetic effects (García et al. 2010; Chaplin et al. 2011a).

5.3 Background fitting

As said before, the low-frequency part of the PSD can be explained by a model in which each source of convective motions is described by an empirical law –initially proposed by Harvey (1985) for the Sun– corresponding to an exponentially decaying time function. To properly fit this convective background, one or two Lorentzian functions are also fitted to take into account for the extra power coming from the p modes (e.g. Vázquez Ramió et al. 2002; Lefebvre et al. 2008) and a constant for the photon noise. Therefore, in the solar case, the model of the global spectrum, including both non-periodic and periodic components, are expressed by:

$$P(\nu) = N_{ph} + \sum_{i=1}^{N} \frac{4\sigma_i^2 \tau_i}{1 + (2\pi\nu\tau_i)^{b_i}} + \sum_{j=1}^{M} A_j \left[\frac{\Gamma_j^2}{(\nu - \nu_{0_j})^2 + \Gamma_j^2} \right]^{c_j} \tag{5.10}$$

where

- $P(\nu)$ is the power spectral density;
- N_{ph} is the photon noise;
- i corresponds to the non-periodic motions;
- j corresponds to the periodic component;
- σ_i and τ_i are respectively the rms-variations and the characteristic time of the i-th background component (the limit of the first sum, N, varies depending on the number of non-periodic background components of the spectrum to fit);

- A_j and ν_{0_j} are the power and the central frequency of the Lorentzian profiles to fit to the periodic components at the higher frequency region of the spectrum, while Γ_j sets its width. These M possible peaks to fit can be identified as the so-called photospheric or/and the chromospheric component;

- finally, c_j (as well as b_i) are decay rates.

In the solar case, and because of the large length of the time series (19 years in the case of SoHO and even longer form GONG and BiSON ground-based networks) it is possible to perform local averages to reduce the number of points while taking into account that the fitting is done in a logarithmic space and thus the points should be equally spaced after doing this transformation.

If signatures of rotation are visible in the PSD at low frequency, it is possible to add a power law and a sequence of Lorentzian peaks at the frequencies of rotation and its harmonics.

An application of the background fit for the Doppler velocity solar spectrum measured by GOLF is shown in Fig. 34. This PSD has been modeled with two non periodic components, one for the granulation and one for the supergranulation, in both cases with the exponent $b_i = 2$. To fit correctly the p-mode envelope measured by GOLF, it is necessary to use 2 Lorentzian profiles instead of 1 (more details can be seen in Lefebvre et al. 2008).

For other stars, thanks to the measurements done by CoRoT and *Kepler* it has been demonstrated that the same approach can be followed even for red giants (Mathur et al. 2011b; Kallinger et al. 2014). For example, in Fig. 35 we represent the background fitting of the two solar analogs 16 Cyg A and B observed by *Kepler* (Metcalfe et al. 2012; Davies et al. 2015).

The analysis of the "ensemble" set of a thousand pulsating red giants of *Kepler* (Mathur et al. 2011b) showed the existence of a relation between the convective parameters and the evolutionary state of the star (e.g. representated by ν_{max}). Theoretical calculations have proven a similar relation and demonstrated the relation between the stellar granulation and the Mach number (Samadi et al. 2013). Moreover, the observational study of the granulation power of red giants, $P_{\rm gran}$ defined as $P_{\rm gran} = 4\sigma^2\tau_{\rm gran}$ uncovered that larger stars present larger intensity fluctuations (see Fig. 36). Part of the reason for this is the smaller total number of granules covering the surface of larger stars, and hence the fluctuations are less averaged, compared to a star with many more (unresolved) granules. We also found that stars in the red clump have very similar values of granulation parameters.

Today, it is of common practice in asteroseismology to fit the background and all the p modes in one step (see e.g. Appourchaux et al. 2008; Ballot et al. 2011; Mathur et al. 2011a). However, in the case of the Sun, this approach is not yet employed because the number of modes –with their associated free parameters–, and the size of the time series –they are too big– make the fitting procedure too slow and with dramatic convergency problems.

5.4 The solar p-mode spectrum as seen by GOLF and VIRGO/SPM

In this section we show an example of the maximum-likelihood fitting procedure (in the frequentist approach) using solar data from SoHO. The analysis presented here has been

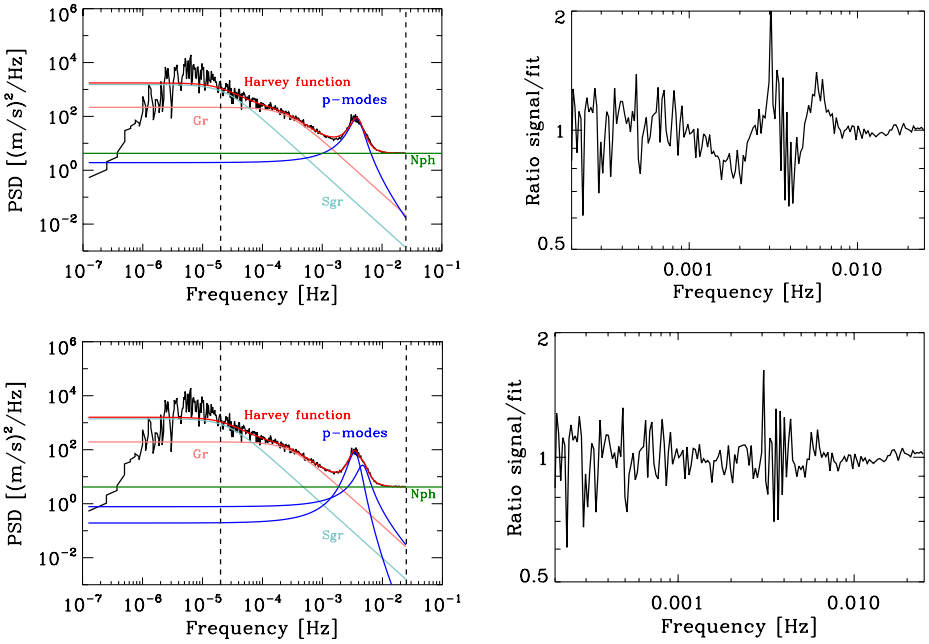

Fig. 34. Results of two different background fits applied to the GOLF spectrum of an arbitrary taken subseries of 91.25 days long. Top: Left, PSD with a fit using 8 parameters (one lorentzian) to adjust the *p*-mode envelope; Right, ratio between the PSD and the fit around the envelope of *p*-modes. Bottom: Left, PSD with a fit using 11 parameters (two lorentzians) to adjust the *p*-mode envelope; Right, ratio between the PSD and the fit around the envelope of *p* modes. The dashed lines represent the range in which the fit is performed. The color used for the different fits are: gray for the super granulation contribution, magenta for the granulation contribution, blue for the *p*-mode envelope, green for the noise and red for the harvey function (the sum of the granulation and supergranulation contributions).

performed over ∼14 years of data collected by GOLF and VIRGO/SPM. 5163 days of GOLF velocity time series from April 11, 1996 to May 30, 2010 with a duty cycle, dc=95.4 % (García et al. 2005); and 5154 days of intensity data from the three VIRGO Sun photometers (SPM) at 402, 500, and 862 nm from April 11, 1996 to May 21, 2010 (dc = 95.2 %). Because the overall noise level of VIRGO/SPM is higher than in GOLF, the frequency range on which we can extract reliable estimates of the p modes at low frequency is reduced (as explained in Sect. 6.4). However, due to the low visibility of the ℓ=3 modes in intensity measurements, the extraction of the p-mode parameters of the ℓ=1 modes could be done up to higher frequencies (∼5000 μHz). The mode blending at high frequency is the limiting factor in radial velocity measurements (see Fig. 32).

To characterize the p modes, we computed the power spectrum density (PSD) of the entire time series in order to maximize the frequency resolution (∼ 2.24 nHz). Therefore, the obtained linewidths of the modes could be slightly overestimated because of the shift

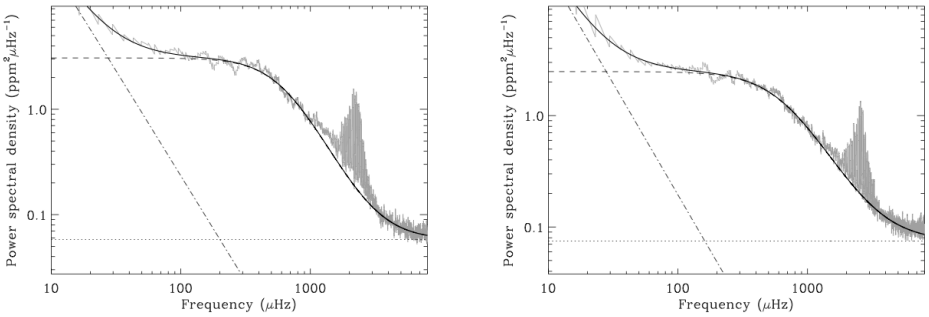

Fig. 35. Background fitting of the two solar analogs 16 Cyg A (left) and B (right) observed by *Kepler*. The PSD has been smoothed by a 20 μHz boxcar (grey), with best-fitting background components attributed to granulation (dashed lines), stellar activity and/or larger scales of granulation (dot- dashed lines) and shot noise (dotted lines), with the sum of the background components plotted as solid black lines. Figure from Metcalfe et al. (2012).

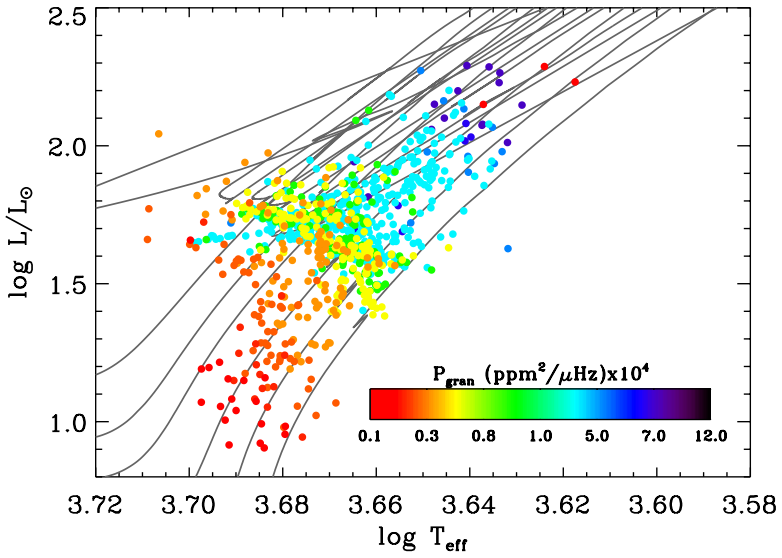

Fig. 36. Distribution of $P_{\rm gran}$ in the HR diagram (color code) for the sample of a thousand red giants observed by *Kepler*. The gray lines represent BaSTI evolutionary tracks computed with solar metallicity. Figure from Mathur et al. (2011b).

of the modes during the solar activity cycle (e.g. Jiménez-Reyes et al. 2003). The fits were performed by orders –fitting separately the odd and even modes– using the methodology

described in the previous sections.

Figures 37 and 38 show the p-mode parameters –large separation, small separation, acoustic power, linewidths, splittings and peak asymmetry– as a function of frequency extracted from GOLF and VIRGO/SPM respectively between 1000 and 4000 μHz, and up to 5000 μHz when possible. The rotation splitting was fixed to 400 nHz for modes above 3500 μHz. Indeed, due to the mode blending, it was impossible to obtain reliable parameters without imposing this additional condition. Thanks to that, we were able to obtain preliminary results of the linewidths extracted from GOLF up to 5000 μHz. Also, as explained before, due to the smaller $\ell = 3$ visibility in the VIRGO/SPM data, the linewidth and acoustic power of the $\ell = 1$ mode could be fitted up to 5000 μHz. Reliable estimates below 1800 μHz could not be properly extracted in VIRGO/SPM data because of the smaller SNR.

The comparison of the large and small separation (Fig. 37 and 38, top panels) with the same quantities computed using the solar seismic model (Turck-Chièze et al. 2001; Mathur et al. 2007), shows that this model is a good reference to look for modes at low frequency. Moreover, the small separations –which are a direct probe of the core of the Sun— are inside one-sigma error bars of those computed with the seismic model. This result was expected because the seismic model has been constructed to minimize the differences with the observations in the deepest regions of the radiative interior and produce the best estimates of the neutrino flux.

We also computed the average maximum amplitude per radial mode of the Sun (Fig 37 bottom right) for the three VIRGO/SPM channels, as it is commonly done in asteroseismology (e.g. Mathur et al. 2010b). The maximum amplitudes were corrected by the instrumental response function using the values given by Michel et al. (2009) for the different channels.

5.5 Ensemble stellar p- and mixed-mode fitting

Kepler allowed to do the first "ensemble" asteroseismic study of many solar-like stars covering a wide range of properties. 61 stars observed during Q5, Q6 and Q7 (from March 22, 2010 till December 22, 2010) were analyzed in an homogeneous way (Appourchaux et al. 2012b). The selected stars are plotted in a seismic HR diagram in Fig. 39.

To properly extract the mode parameters for these stars, we separate them into three different categories: simple (sun-like), F-like, and sub giants (stars having $\ell = 1$ mixed modes). Out of the 61 stars, we have 28 simple stars, 15 F-like stars, and 18 mixed-mode stars. Figure 39 shows that the boundary between simple stars and F-like stars is about 6400 K which roughly corresponds to a linewidth at maximum mode height of about 4 μHz (Appourchaux et al. 2012a). For these F-like stars, the frequency separation between the $l = 0$ and $l = 2$ modes (i.e. small separation) ranges from 4 μHz to 12 μHz combined with a linewidth of at least 4 μHz justifies why the detection of the $\ell = 0, 2$ ridge is more difficult for these stars (see also Benomar et al. 2009a). Examples of the three kind of stars are shown in Fig. 40.

Nowadays, the efforts are concentrated in the proper fitting of red giants. The first challenge is to properly identify the modes to be fitted. To do so, several semi-analytical models have been developed (e.g. Mosser et al. 2012b; Goupil et al. 2013) that allow a

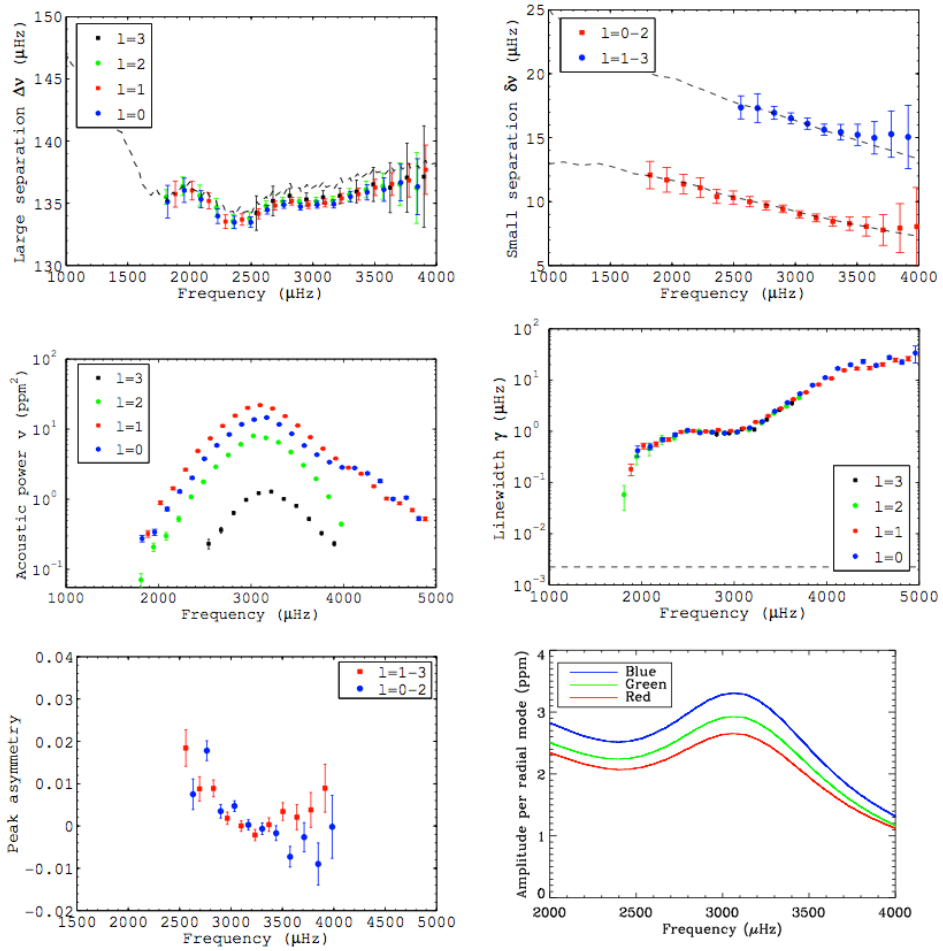

Fig. 37. Top left: large separation as a function of frequency calculated from the fitted VIRGO/SPM frequencies. Top right: small separation. Middle left: Full amplitudes (in units of ppm^2). Middle right: Linewidths (in μHz). Bottom left: Asymmetry. Bottom right: average maximum rms amplitudes per radial mode for the three VIRGO/SPM channels. Due to the small $\ell = 3$ visibility in the VIRGO/SPM data, these modes do not perturb the $\ell = 1$ and the linewidth and acoustic power of the $\ell = 1$ modes could be fitted up to 5000 μHz.

first proper identification of the modes if the rotational splittings are not too big. Once this identification is done, bayesian techniques are more suited to this problem, and thus the first ensemble fit of 19 young red giants has been performed (Corsaro et al. 2015). The second challenge that the community will need to face in the near future will be how to do these fits in the more than 30,000 red giants measured by CoRoT and *Kepler* missions.

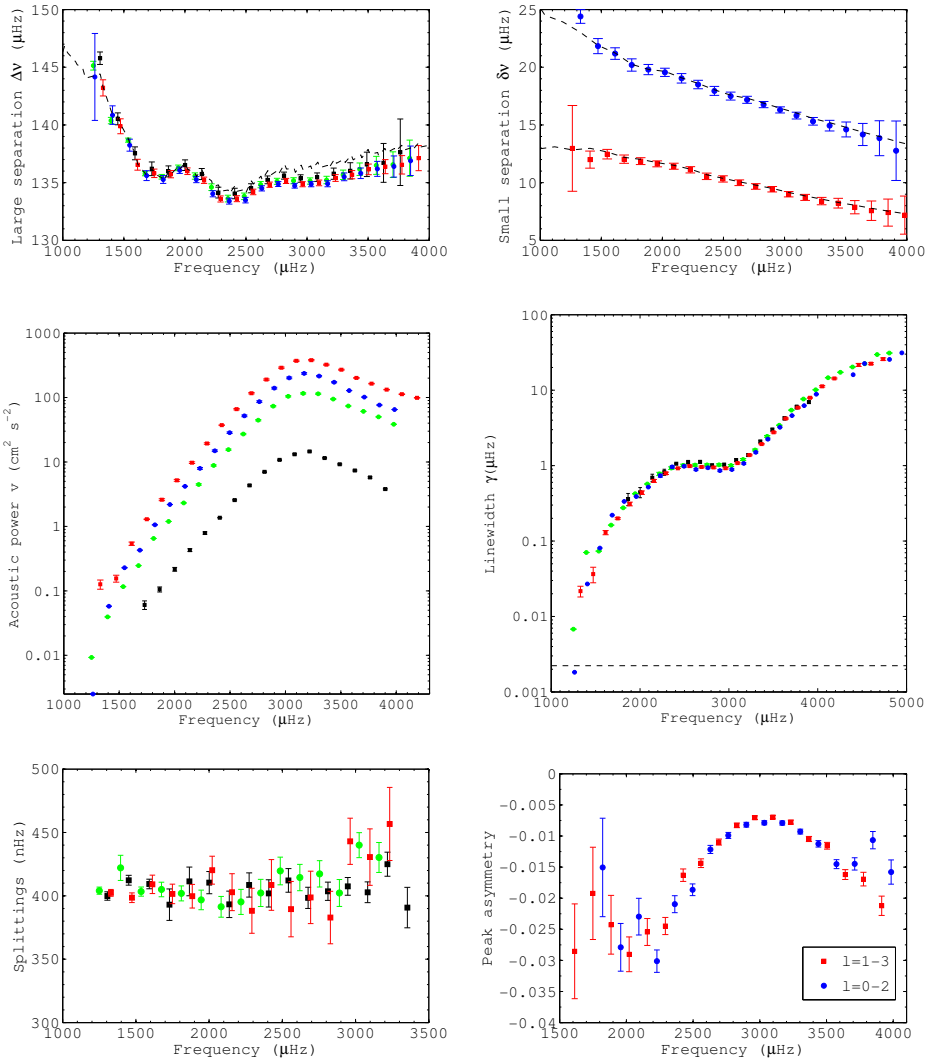

Fig. 38. Top left: large separation as a function of frequency calculated from the fitted GOLF frequencies (same legend than in previous figure (37). The formal errors were multiplied by a factor 10. The dashed lines correspond to the theoretical values using the Saclay seismic model Mathur et al. (2007). Top right: small separation ($\ell = 0 - 2$ modes in red, $\ell = 1 - 3$ modes in blue). The formal errors were multiplied by a factor 10. Middle left: Full amplitudes (in units of cm^2 s^{-2}). Middle right: Linewidths (in μHz). The horizontal dashed line corresponds to the frequency resolution. Bottom left: splittings. Above 3500 μHz, the splittings were fixed to 400 nHz. Bottom right: Asymmetry. The increase below 2000 μHz could not be real due to the reduction in the SNR and the fewer number of points defining the profile.

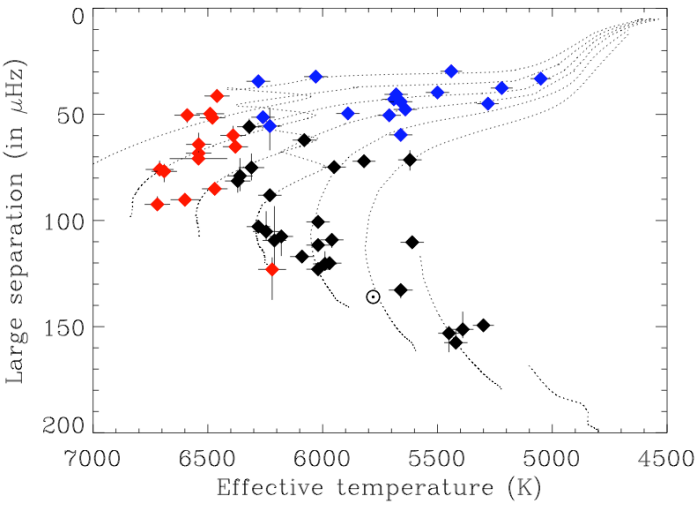

Fig. 39. Seismic HR diagram in which the large separation is plotted versus the effective temperature of 61 solar-like stars observed by *Kepler*: (black) simple stars, (blue) mixed-mode stars, (red) F-like stars, (⊙) our Sun. The uncertainties on the large separation represent the minimum and maximum variation with respect to the median; some of these uncertainties are within the thickness of symbol. The evolutionary tracks for stars of mass 0.8 $M_\odot$ (most right) to 1.5 $M_\odot$ (most left) (by step of 0.1 $M_\odot$) are shown as dotted lines. The tracks are derived from Marigo et al. (2008). Figure from Appourchaux et al. (2012b).

6 Instrumentation

As a consequence of the stellar oscillations, the gas is compressed and expanded in the photosphere. With each cyclic movement, the brightness of the star fluctuates. In the compression it warms up while in the expansions it cools down. As a consequence, the stellar flux is modulated and this modulation can be measured. At the same time, and due to the movement of the stellar photosphere, the absorption lines are also Doppler shifted. Stellar oscillations can then be measured as a periodic variation of the total stellar flux or by measuring the cyclic Doppler shifts induced by the pulsations. However, the magnitude of such variations are really small: around 15 cm/s at $\nu_{\rm max}$ for the velocity shifts and around 3×10^{-6} for brightness variations, corresponding to 10^{-3} K in temperature. It is also important to notice that solar oscillations were also looked for by measuring variations in the solar diameter using the SCLERA experiment (Santa Catalina Laboratory for Experimental Relativity by Astrometry, Hill et al. 1976), and using the CNES mission PICARD (Thuillier et al. 2006). Unfortunately, the complexity of this type of observations prevented the success of such measurements.

Due to this small intrinsic amplitude of the oscillations, precise and stable instrumentation are required to reach the high SNR necessary to properly record the solar and stellar

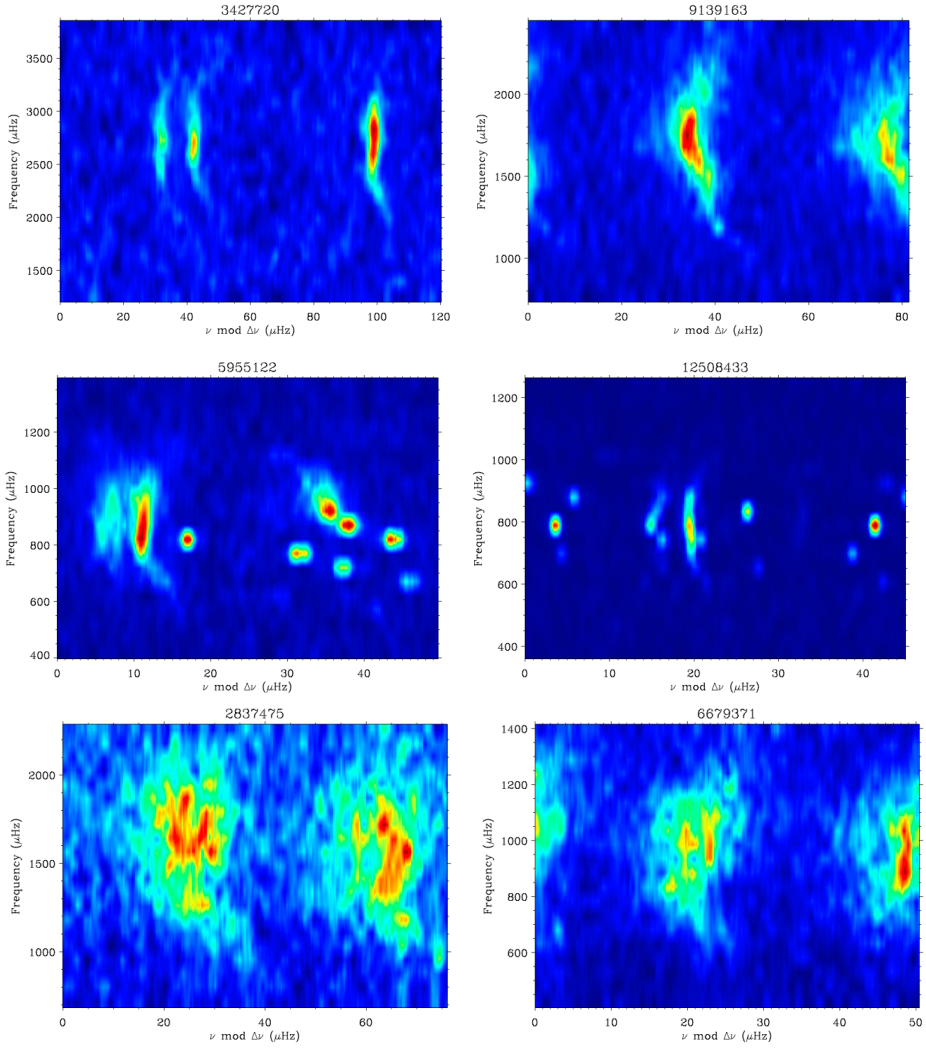

Fig. 40. Example of échelle diagrams corresponding to the "ensemble" analysis of 61 solar-like *Kepler* stars studied by Appourchaux et al. (2012b). On top two simple stars, in the middle two mixed-mode stars, and two F-like stars in the bottom panels. The power spectra are normalized by the background and smoothed over 3 μHz. The échelle diagrams are smoothed over 2 orders in the vertical direction. Figures from Appourchaux et al. (2012b).

pulsations.

Helio- and Astero-seismic observations can be performed either form the ground and from space. Because of the intrinsic requirement on the continuity of the measurements from weeks to months and years, it seems clear that single site observations from ground

are not good (excepting the sites placed close to the Earth's Poles). The day-night cycle imposes a window function of around 8-12h which introduces daily aliases at a frequency of 11.57 μHz in the spectral analysis. To avoid this problem, ground-based networks has been built and are currently running (e.g. GONG or BiSON).

Apart form the magnitude used to measure the stellar oscillations, we can classify the helioseismic instruments in imaged and Sun-as-a-star ones. Due to the nature of this review, we will concentrate only on non-imaged instrumentation. I have chosen some instruments as examples of the techniques that I will explain in more details here. For a more exhaustive review on all the past, present, and future instrumentation in helio and asteroseismology, I recommend the reader the reviews by Appourchaux & Grundahl (2015) and Pallé et al. (2015).

6.1 Helioseismic Doppler velocity instruments

Helioseismic Doppler velocity measurements are complicate in nature because the sensitivity of the measurement is not uniform across the solar disk due to the projection effect combined with the solar rotation. A theoretical calculation of such sensitivity for the case of the GOLF instrument can be found in García et al. (1998b).

Helioseismology entered in a new era in the mid nineties with the deployment of the ground based networks around the world such as the Birmingham Solar Oscillation Network (BiSON, Chaplin et al. 1996), the Global Oscillation Network Group (GONG, Harvey et al. 1996), and the launch of the Solar and Heliospheric Observatory (SoHO) mission (Domingo et al. 1995). All these facilities allowed a continuous monitoring of the Sun, drastically improving the quality of the datasets available.

The SoHO mission is a three-axis, stabilized spacecraft developed by the European Space Agency (ESA) in collaboration with the National Aeronautics and Space Administration (NASA). It contains eleven scientific instruments dedicated to the study of the Sun, its heliosphere and the solar wind (Domingo et al. 1995). SoHO was one of the cornerstones of the ESA Space Science program called Horizon 2000 and it was successfully launched in December 1995.

SoHO offers an unprecedented opportunity to study the deep interior of the Sun through helioseismology under ideal conditions at the Lagrange L_1 point at 1.5 10^6 km from Earth. At this location, no terrestrial atmospheric effects are present, continuous exposures to the Sun are possible (more than 95% duty cycle), and there is a low Sun-spacecraft line-of-sight velocity. This spacecraft carries three Helioseismic instruments, two using Doppler velocity techniques: GOLF[3] and SOI/MDI[4], and one recording brightness variations: VIRGO[5].

The two main Doppler velocity instruments performing Sun-as-a-star observations, BiSON and GOLF/SoHO are based on the same technique, the spectrophotometry. GOLF was originally designed to measure the disk-integrated —Sun-as-a-star— oscillations of the Sun (e.g. Lazrek et al. 1997; Thiery et al. 2000; García et al. 2001) and its mean

[3]Global Oscillations at Low Frequency (Gabriel et al. 1995)
[4]Solar Oscillation Imager/Michelson Doppler Interferometer (Scherrer et al. 1995)
[5]Variability of solar Irradiance and Gravity Oscillations (Fröhlich et al. 1995)

magnetic field (García et al. 1999a). The main scientific objective of both experiments is the quantitative knowledge of the internal structure of the Sun by measuring the spectrum of its global oscillations in a wide frequency range (30 nHz to 25 mHz). In the case of GOLF, with special interest in detecting the low-degree acoustic (p) and gravity (g) modes (located at low frequencies below 1.5 mHz).

GOLF is an improved resonant scattering spectrophotometer that determines the line-of-sight velocity of the integrated visible solar surface of the Sun by measuring the Doppler shift of the neutral sodium doublet (D_1 at λ= 589.6 nm and D_2 at λ = 589.0 nm). BiSON used the potassium Fraunhofer line at 770 nm instead.

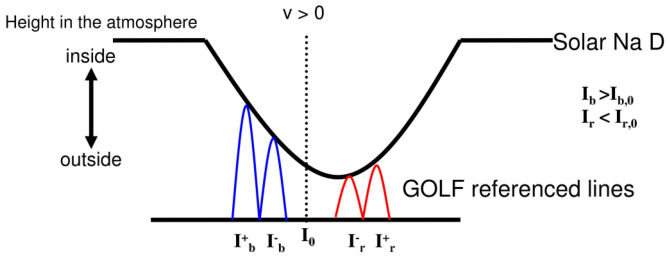

Fig. 41. Representation of the GOLF measurements. The Solar Na D line is displaced from the rest position due to a positive velocity ($V > 0$). The BW (blue wing) measures higher in the line, which means deeper (close to the photosphere) in the solar atmosphere. The RW (red wing) measures closer to the bottom of the line, i.e. upper in the solar atmosphere.

In the GOLF instrument, the light coming from the solar sodium absorption line (half-width ∼500 mÅ) traverses a sodium vapour cell –placed in a longitudinal magnetic field of ∼5000 Gauss– which has an intrinsic (thermal) absorption line-width of the order of 25 mÅ, where it is absorbed and re-emitted in all directions. This scattered light is symmetrically split into its Zeeman components displaced around ± 108 mÅ from the rest wavelength, allowing a measurement on either side on the wings of the solar absorption profile. The sodium cell is surrounded by a coil that changes the magnetic field ± 100 Gauss allowing the measurement of two different points on each wing (see Fig. 41). A polarization mechanism placed in the optical path prior to the vapor cell selects the circular polarization of the entrance light and switches every 10s between both wings. A Doppler displacement of the solar Na line will be seen as a different intensity on each wing of the instrument and thus the ratio $(I_b - I_r)/(I_b + I_r)$ will be proportional to this velocity (see Fig. 41). The scattered photons are collected by 2 photomultiplier tubes. Redundancy on both, the electronics and photomultipliers guarantees the long term efficiency of the detection subsystem. A complete description of the instrument can be found in (Gabriel et al. 1995, 1997).

6.2 Helioseismic photometric observations

The closest helioseismic observations to the ones commonly done in asteroseismology are those performed by the VIRGO package aboard SoHO. It is composed of 3 types

of instruments including absolute radiometers, an imager, and 3 sun photometers (SPM, Fröhlich et al. 1995), centered at 402 nm (blue), 500 nm (green), and 862 nm (red). Basri et al. (2010) demonstrated that the sum of these two last channels (green and red) is a good photometric approximation of the *Kepler* bandwidth.

6.3 Stellar instrumentation

As already said in the introduction of this chapter, asteroseismology showed its potential with the development of space instrumentation. After the pioneering measurements done with WIRE (Wide-Field Infrared Explorer, Buzasi et al. 2000) and the Canadian MOST satellite (Microvariability and Oscillations of Stars, Matthews et al. 2000), space asteroseismology reached a golden age with the observations performed by CoRoT (Convection, Rotation and planetary Transits, Baglin et al. 2006) and *Kepler* (Borucki et al. 2010; Koch et al. 2010). The future is even more promising than the present with the on-going K2 mission (Howell et al. 2014), and the future missions such as TESS (Transiting Exoplanet Survey Satellite, Ricker et al. 2014) and PLATO (Rauer et al. 2014). A comparison of the asteroseismic dedicated satellites is shown in Table 1.

Table 1.

Mission	Launch	D (cm)	FOV (deg × deg)	m_V	Number of stars per field	Total Number of stars
MOST	2003	15	0.4 × 0.4	<6	1	150
CoRoT	2006	27	2.8 × 2.8	<7	12,000	150,000
Kepler	2009	95	10.5 × 10.5	<12	206,000	206,000
K2	2014	95	10.5 × 10.5	<12	~20,000	~160,000
Brite	2013	3	24 × 24	<4	15-40	~500
TESS	2017	10	23 × 90	<12	20,000	500,000
PLATO	2024	67	47 × 47	<13	100,000	1,000,000

While I am writing this chapter, the analysis of the first K2 solar-like pulsating stars is being conducted and global seismic properties have been measured in some of the targets in Campaign one. In the rest of the chapter I will give a brief overview of the two main space missions CoRoT and *Kepler*.

6.3.1 CoRoT

The CNES-ESA mission CoRoT (Convection, Rotation and planetary Transits), launched on December 27, 2006, has been the first dedicated asteroseismic mission that has been able to perform ultra-high precision, wide-field, relative stellar photometry, for very long continuous observing runs (up to 150 days) on the same field of view. On June 17, 2014 CoRoT received the last telecommand from Earth after ~ 7 year in-orbit performing scientific activities, establishing the official end of the mission.

CoRoT was led by the french space agency, CNES, in association with other french laboratories and with a significant international participation. Indeed, Austria, Belgium, Germany and ESA (Science Program and RSSD/ESTEC) contributed to the payload,

whereas Spain and Brazil contributed to the ground segment. CoRoT had two main scientific programs working simultaneously on adjacent regions of the sky: asteroseismology, and the search for exoplanets using the transiting method.

CoRoT had a 27-cm afocal telescope producing an image of the stellar field into 4 CCDs (composed by a matrix of 2048 x 4096 pixels) and installed in a proteus platform. Each CCD was working on a frame transfer mode, two optimized for asteroseismology and the other two, for exoplanet research (see Fig. 42). The images on the seismo CCDs were defocused to minimize the effects of the spacecraft jitter. Thus, stellar fluxes were measured every second with a dead time of 0.206s (sampling cycle of 79.4 %). The data was finally integrated to a cadence of 32s in the case of the seismo filed. For the exoplanet field, the nominal integration time was also 32s but the flux of 16 read-outs was co-added on an 8.5 min cadence before being downlinked to Earth. Moreover, 500 targets per CCD preserved the nominal sampling time of 32 sec to allow a better transiting timing. These were known as "oversampled" light curves. At the beginning of each run, 1000 targets were selected for oversampling, but this list of targets was updated every week, thanks to a quick look analysis of the light curves.

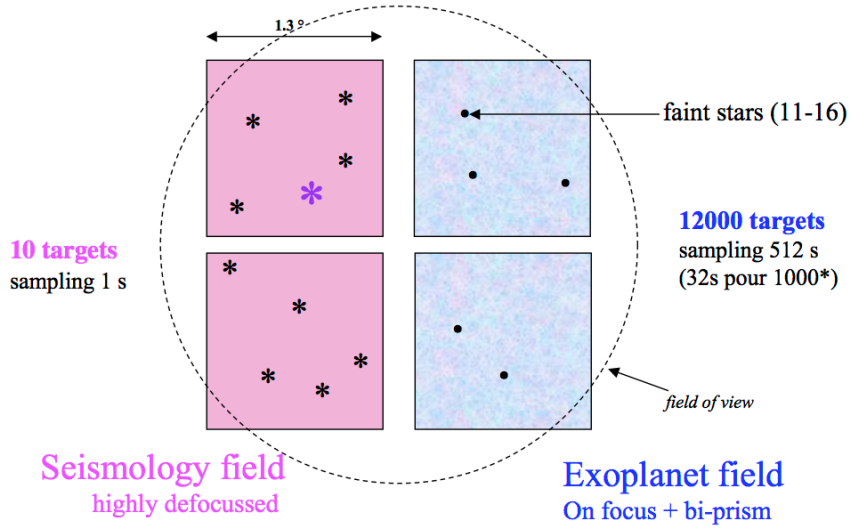

Fig. 42. Focal plane of the CoRoT instrument. At any time, around 10 targets are observed in the seismology field, while ~ 12000 are monitored in the exoplanet one.

To prevent the instrument from being blinded by the Sun and to keep the scattered light by the Earth at a minimum level, CoRoT could only observe into two 10° almost circular regions pointing towards the galactic center and the anticenter in the equatorial plane. These regions were called the "CoRoT eyes" (see Fig. 43). These positions were selected as a good compromise between the stellar density required for exoplanet research and the existence of seismically interesting targets. A small drift of the orbit allowed to

optimize the observing conditions for fields at the edge of the circle and slightly extend these continuous viewing zones during the lifetime of the CoRoT mission.

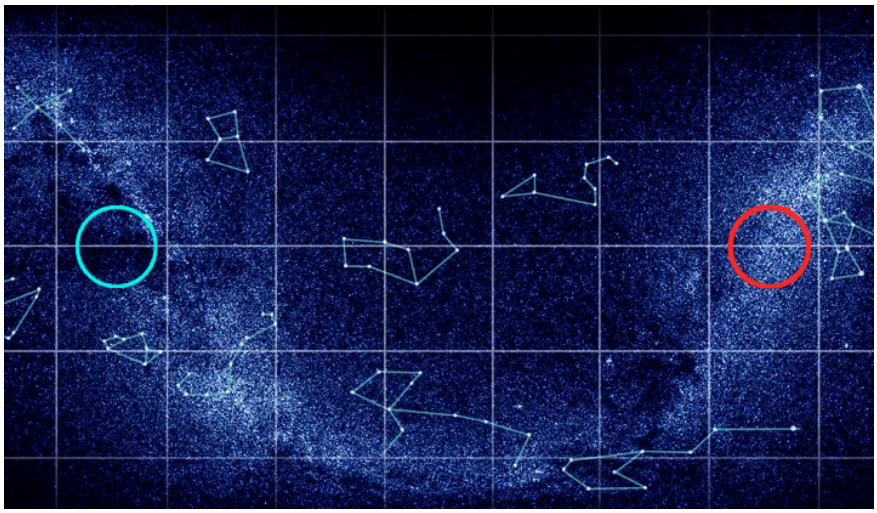

Fig. 43. Regions of the sky in which CoRoT could point, usually known as the "CoRoT eyes".

Every six months (in April and October), the satellite were rotated by 180° with respect to the polar axis and a new observation period started in the opposite direction. The longest periods of continuous observation were 150 days, the so-called Long Runs, ensuring the highest expected scientific return. Between two long runs, other fields were observed for a much shorter period of around a maximum of 25 days (Short Run). Due to a malfunction of one module (two CCDs, one on each scientific program) in 2009, we lost half of the CoRoT field of view. Then a new strategy were designed, observing the main seismo target during roughly three months and then rotating the satellite but keeping this main target in view for another three months. In such way, we had a long run of the main target in the seismo field while the stars in the exo channel changed to maximize the detection probability.

6.3.2 *Kepler*

Observational astroseismology reaches its maturity with the launch of *Kepler* on March 7, 2009 (GMT) (Borucki et al. 2010; Koch et al. 2010). It was a NASA discovery mission whose primary goal was the search for and characterization of extrasolar planetary systems. This was accomplished by time-series photometry of around 206,000 stars in a single field of view of 115 deg^2 –selected to provide the optimal density of stars for extrasolar planet research– and located in the constellation of Cygnus and Lyra. The loss of two reaction wheels on the *Kepler* spacecraft has ended the primary mission data collection after $\sim$ 4 years of continuous operations. After a hard effort, engineers at NASA demonstrated the viability of a new mission, called K2, in which *Kepler* could observe

target fields along a narrow band around the ecliptic for 2 to 3 more years (Howell et al. 2014). The first fields have already been observed and the results are very promising from the asteroseismic of solar-like stars point of view (Angus et al. 2015; Chaplin et al. 2015; Stello et al. 2015).

The *Kepler* main scientific objective was to measure Earth-like planets in an Earth-like orbit around Sun-like stars inside the habitable zone. The very precise photometry required for the planet search also provided excellent data for asteroseismology. While most stars were observed at a cadence of 30 min, some of them (around 512 at any time), were observed at a cadence of 1 min (Gilliland et al. 2010; Jenkins et al. 2010). Combining the stars observed at both cadences it was possible to observe pulsating stars covering most of the regions in the HR diagram. Short-cadence data allowed the characterization of about 500 solar-like pulsating stars (Chaplin et al. 2011c), while using long cadence data, measurements of more than 13,000 red giants were possible (Stello et al. 2013).

6.4 Comparison between Doppler velocity and Intensity measurements

Thanks to SoHO we can directly compare the resultant power spectrum obtained from Doppler velocity variations measured by GOLF and by measuring the intensity variations form the Sun spectrophotometers (SPM) of the VIRGO package. In Fig. 44 the PSD obtained using both instruments is shown. We have normalized both spectrum in such a way that the maximum of the p-mode hump has the same amplitude. The convective background in intensity is higher than in velocity, which make it difficult to detect and characterize the low-order p modes below 1.8 mHz. Moreover, the signal-to-background ratio of the p modes for intensity measurements is not better than 30, while in velocity it is common to reach a level of 300.

Thus the future challenge of asteroseismology will be to observe hundred thousands of stars in Doppler velocity and from the space... But a long way is in front of us before developing such instrumentation.

References

Anguera Gubau, M., Palle, P. L., Perez Hernandez, F., Regulo, C., & Roca Cortes, T. 1992, A&A, 255, 363

Angus, R., Foreman-Mackey, D., & Johnson, J. A. 2015, ArXiv 1505.07105

Appourchaux, T. 2003, A&A, 412, 903

Appourchaux, T. 2014, A crash course on data analysis in asteroseismology, ed. P. L. Pallé & C. Esteban, 123

Appourchaux, T., Belkacem, K., Broomhall, A., et al. 2010, A&A Rev., 18, 197

Appourchaux, T., Benomar, O., Gruberbauer, M., et al. 2012a, A&A, 537, A134

Appourchaux, T., Chaplin, W. J., García, R. A., et al. 2012b, A&A, 543, A54

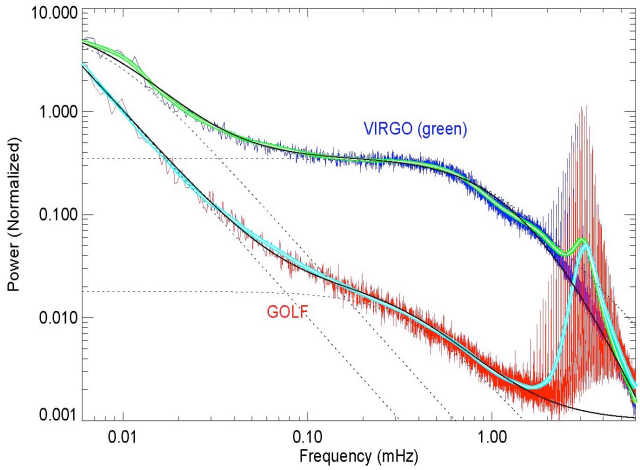

Fig. 44. Comparison between the PSD extracted from Doppler velocity (GOLF) or intensity measurements (VIRGO/SPM green channel). The fitting to the convective background is also shown. (Credits, T. Bedding & H. Kjeldsen).

Appourchaux, T., Gizon, L., & Rabello-Soares, M.-C. 1998, A&AS, 132, 107

Appourchaux, T. & Grundahl, F. 2015, Extraterrestrial Seismology, ed. V. C. H. Tong & R. A. García (Cambridge University Press)

Appourchaux, T., Leibacher, J., & Boumier, P. 2007, A&A, 463, 1211

Appourchaux, T., Michel, E., Auvergne, M., et al. 2008, A&A, 488, 705

Auvergne, M., Bodin, P., Boisnard, L., et al. 2009, A&A, 506, 411

Baglin, A., Auvergne, M., Boisnard, L., et al. 2006, in COSPAR, Plenary Meeting, Vol. 36, 36th COSPAR Scientific Assembly, 3749

Ballot, J., Appourchaux, T., Toutain, T., & Guittet, M. 2008, A&A, 486, 867

Ballot, J., García, R. A., & Lambert, P. 2006, MNRAS, 369, 1281

Ballot, J., Gizon, L., Samadi, R., et al. 2011, A&A, 530, A97

Barban, C., Deheuvels, S., Baudin, F., et al. 2009, A&A, 506, 51

Basri, G., Walkowicz, L. M., Batalha, N., et al. 2010, ApJ Lett., 713, L155

Basri, G., Walkowicz, L. M., & Reiners, A. 2013, ApJ, 769, 37

Basu, S., Chaplin, W. J., Elsworth, Y., New, R., & Serenelli, A. M. 2009, ApJ, 699, 1403

Basu, S., Christensen-Dalsgaard, J., Chaplin, W. J., et al. 1997, MNRAS, 292, 243

Basu, S., Grundahl, F., Stello, D., et al. 2011, ApJ Lett., 729, L10

Batalha, N. M., Borucki, W. J., Bryson, S. T., et al. 2011, ApJ, 729, 27

Baudin, F., Barban, C., Belkacem, K., et al. 2011, A&A, 529, A84

Bayes, T. 1763, Philosophical Transactions of the Royal Society of London, 53, 370

Bazot, M. & Vauclair, S. 2004, A&A, 427, 965

Bazot, M., Vauclair, S., Bouchy, F., & Santos, N. C. 2005, A&A, 440, 615

Beck, P. G., Bedding, T. R., Mosser, B., et al. 2011, Science, 332, 205

Beck, P. G., Montalban, J., Kallinger, T., et al. 2012, Nature, 481, 55

Bedding, T. R. & Kjeldsen, H. 2003, Publications of the Astronomical Society of Australia, 20, 203

Bedding, T. R., Kjeldsen, H., Campante, T. L., et al. 2010, ApJ, 713, 935

Bedding, T. R., Mosser, B., Huber, D., et al. 2011, Nature, 471, 608

Belkacem, K., Goupil, M. J., Dupret, M. A., et al. 2011, A&A, 530, A142

Belkacem, K., Samadi, R., Mosser, B., Goupil, M.-J., & Ludwig, H.-G. 2013, in Astronomical Society of the Pacific Conference Series, Vol. 479, Astronomical Society of the Pacific Conference Series, ed. H. Shibahashi & A. E. Lynas-Gray, 61

Benomar, O., Appourchaux, T., & Baudin, F. 2009a, A&A, 506, 15

Benomar, O., Baudin, F., Campante, T. L., et al. 2009b, A&A, 507, L13

Borucki, W. J., Koch, D., Basri, G., et al. 2010, Science, 327, 977

Borucki, W. J., Koch, D. G., Batalha, N., et al. 2012, ApJ, 745, 120

Bracewell, R. N. 2000, The Fourier transform and its applications

Brown, T. M. & Christensen-Dalsgaard, J. 1990, ApJ, 349, 667

Brown, T. M., Gilliland, R. L., Noyes, R. W., & Ramsey, L. W. 1991, ApJ, 368, 599

Brun, A. S., Miesch, M. S., & Toomre, J. 2004, ApJ, 614, 1073

Buzasi, D., Catanzarite, J., Laher, R., et al. 2000, ApJ Lett., 532, L133

Campante, T. L. 2012, PhD thesis, PhDT Thesis, Universidade do Porto

Campante, T. L., Barclay, T., Swift, J. J., et al. 2015, ApJ, 799, 170

Campante, T. L., Handberg, R., Mathur, S., et al. 2011, A&A, 534, A6

Carrier, F., Eggenberger, P., & Bouchy, F. 2005, A&A, 434, 1085

Chaplin, W., J. 2006, Music of the Sun: Story of Helioseismology (Oneworld Publications)

Chaplin, W. J., Appourchaux, T., Baudin, F., et al. 2006, MNRAS, 369, 985

Chaplin, W. J., Appourchaux, T., Elsworth, Y., et al. 2010, ApJ Lett., 713, L169

Chaplin, W. J., Bedding, T. R., Bonanno, A., et al. 2011a, ApJ Lett., 732, L5

Chaplin, W. J., Christensen-Dalsgaard, J., Elsworth, Y., et al. 1999a, MNRAS, 308, 405

Chaplin, W. J., Elsworth, Y., Davies, G. R., et al. 2014, MNRAS, 445, 946

Chaplin, W. J., Elsworth, Y., Howe, R., et al. 1996, Sol. Phys., 168, 1

Chaplin, W. J., Elsworth, Y., Isaak, G. R., et al. 2001, MNRAS, 322, 22

Chaplin, W. J., Elsworth, Y., Isaak, G. R., Miller, B. A., & New, R. 1999b, MNRAS, 308, 424

Chaplin, W. J., Elsworth, Y., Isaak, G. R., Miller, B. A., & New, R. 2000, MNRAS, 313, 32

Chaplin, W. J., Houdek, G., Karoff, C., Elsworth, Y., & New, R. 2009, A&A, 500, L21

Chaplin, W. J. & Howe, R. 2015, Extraterrestrial Seismology (Cambridge University Press)

Chaplin, W. J., Kjeldsen, H., Bedding, T. R., et al. 2011b, ApJ, 732, 54

Chaplin, W. J., Kjeldsen, H., Christensen-Dalsgaard, J., et al. 2011c, Science, 332, 213

Chaplin, W. J., Lund, M. N., Handberg, R., et al. 2015, ArXiv 1507.01827

Christensen-Dalsgaard, J. 2002a, Reviews of Modern Physics, 74, 1073

Christensen-Dalsgaard, J. 2002b, Reviews of Modern Physics, 74, 1073

Christensen-Dalsgaard, J. 2004, Sol. Phys., 220, 137

Christensen-Dalsgaard, J., Bedding, T. R., & Kjeldsen, H. 1995, ApJ Lett., 443, L29

Christensen-Dalsgaard, J. & Berthomieu, G. 1991, Theory of solar oscillations. (Solar Interior and Atmosphere), 401–478

Christensen-Dalsgaard, J., Gough, D., & Toomre, J. 1985, Science, 229, 923

Christensen-Dalsgaard, J. & Gough, D. O. 1976, Nature, 259, 89

Christensen-Dalsgaard, J. & Houdek, G. 2010, Ap&SS, 328, 51

Christensen-Dalsgaard, J., Kjeldsen, H., Brown, T. M., et al. 2010, ApJ Lett., 713, L164

Christiansen, J. L., Jenkins, J. M., Caldwell, D. A., et al. 2013, Kepler Data Characteristics Handbook, Tech. Rep. KSCI-19040-004, NASA

Claverie, A., Isaak, G. R., McLeod, C. P., van der Raay, H. B., & Cortes, T. R. 1979, Nature, 282, 591

Corsaro, E., De Ridder, J., & García, R. A. 2015, A&A, 579, A83

Corsaro, E., Stello, D., Huber, D., et al. 2012, ApJ, 757, 190

Couvidat, S., García, R. A., Turck-Chièze, S., et al. 2003, ApJ Lett., 597, L77

Cox, J. P. 1980, Theory of stellar pulsation

Davies, G. R., Broomhall, A. M., Chaplin, W. J., Elsworth, Y., & Hale, S. J. 2014, MNRAS, 439, 2025

Davies, G. R., Chaplin, W. J., Farr, W. M., et al. 2015, MNRAS, 446, 2959

Deheuvels, S., Bruntt, H., Michel, E., et al. 2010, A&A, 515, A87

Deheuvels, S., Doğan, G., Goupil, M. J., et al. 2014, A&A, 564, A27

Deheuvels, S., García, R. A., Chaplin, W. J., et al. 2012, ApJ, 756, 19

Deubner, F.-L. 1975, A&A, 44, 371

Domingo, V., Fleck, B., & Poland, A. I. 1995, Sol. Phys., 162, 1

Duez, V., Mathis, S., & Turck-Chièze, S. 2010, MNRAS, 402, 271

Dupret, M., Belkacem, K., Samadi, R., et al. 2009, A&A, 506, 57

Duvall, Jr., T. L. 1990, in Astrophysics and Space Science Library, Vol. 159, IAU Colloq. 121: Inside the Sun, ed. G. Berthomieu & M. Cribier, 253

Dziembowski, W. A. & Pamyatnykh, A. A. 1991, A&A, 248, L11

Eddington, A. S. 1926, The Internal Constitution of the Stars

Eff-Darwich, A. & Korzennik, S. G. 2013, Sol. Phys., 287, 43

Eff-Darwich, A., Korzennik, S. G., Jiménez-Reyes, S. J., & García, R. A. 2008, ApJ, 679, 1636

Eggenberger, P., Meynet, G., Maeder, A., et al. 2010, A&A, 519, A116

Elad, M., Starck, J.-L., Querre, P., & Donoho, D. 2005, J. on Applied and Computational Harmonic Analysis, 19, 340

Elsworth, Y., Howe, R., Isaak, G. R., et al. 1994, MNRAS, 269, 529

Elsworth, Y., Howe, R., Isaak, G. R., et al. 1995, Nature, 376, 669

Evans, J. W. & Michard, R. 1962, ApJ, 136, 493

Fahlman, G. G. & Ulrych, T. J. 1982, MNRAS, 199, 53

Fletcher, S. T., Broomhall, A., Salabert, D., et al. 2010, ApJ Lett., 718, L19

Foster, G. 1995, AJ, 109, 1889

Fröhlich, C., Romero, J., Roth, H., et al. 1995, Sol. Phys., 162, 101

Gabriel, A. H., Baudin, F., Boumier, P., et al. 2002, A&A, 390, 1119

Gabriel, A. H., Charra, J., Grec, G., et al. 1997, Sol. Phys., 175, 207

Gabriel, A. H., Grec, G., Charra, J., et al. 1995, Sol. Phys., 162, 61

García, R. A. & Ballot, J. 2008, A&A, 477, 611

García, R. A., Boumier, P., Charra, J., et al. 1999a, A&A, 346, 626

García, R. A., Ceillier, T., Salabert, D., et al. 2014a, A&A, 572, A34

García, R. A., Corbard, T., Chaplin, W. J., et al. 2004, Sol. Phys., 220, 269

García, R. A., Hekker, S., Stello, D., et al. 2011, MNRAS, 414, L6

García, R. A., Jefferies, S. M., Toner, C. G., & Pallé, P. L. 1999b, A&A, 346, L61

García, R. A., Jiménez, A., Mathur, S., et al. 2008a, Astronomische Nachrichten, 329, 476

García, R. A., Mathur, S., & Ballot, J. 2008b, Sol. Phys., 251, 135

García, R. A., Mathur, S., Ballot, J., et al. 2008c, Sol. Phys., 251, 119

García, R. A., Mathur, S., González Hernández, I., & Jiménez, A. 2009, in Astronomical Society of the Pacific Conference Series, Vol. 416, Solar-Stellar Dynamos as Revealed by Helio- and Asteroseismology: GONG 2008/SOHO 21, ed. M. Dikpati, T. Arentoft, I. González Hernández, C. Lindsey, & F. Hill, 297

García, R. A., Mathur, S., Pires, S., et al. 2014b, A&A, 568, A10

García, R. A., Mathur, S., Salabert, D., et al. 2010, Science, 329, 1032

García, R. A., Pallé, P. L., Turck-Chièze, S., et al. 1998a, ApJ Lett., 504, L51

García, R. A., Pérez Hernández, F., Benomar, O., et al. 2014c, A&A, 563, A84

García, R. A., Régulo, C., Turck-Chièze, S., et al. 2001, Sol. Phys., 200, 361

García, R. A., Roca Cortés, T., & Régulo, C. 1998b, A&AS, 128, 389

García, R. A., Turck-Chièze, S., Boumier, P., et al. 2005, A&A, 442, 385

García, R. A., Turck-Chièze, S., Jiménez-Reyes, S. J., et al. 2007, Science, 316, 1591

Gaulme, P., Deheuvels, S., Weiss, W. W., et al. 2010, A&A, 524, A47

Gilliland, R. L., Jenkins, J. M., Borucki, W. J., et al. 2010, ApJ Lett., 713, L160

Gizon, L. & Solanki, S. K. 2003, ApJ, 589, 1009

Goldreich, P. & Keeley, D. A. 1977, ApJ, 212, 243

Goldreich, P. & Kumar, P. 1988, ApJ, 326, 462

Gough, D. O. 1985, in ESA SP-235: Future Missions in Solar, Heliospheric & Space Plasma Physics, ed. E. Rolfe & B. Battrick, 183

Gough, D. O., Kosovichev, A. G., Toomre, J., et al. 1996, Science, 272, 1296

Goupil, M. J., Mosser, B., Marques, J. P., et al. 2013, A&A, 549, A75

Grec, G., Fossat, E., & Pomerantz, M. 1980, Nature, 288, 541

Haas, M. R., Batalha, N. M., Bryson, S. T., et al. 2010, ApJ Lett., 713, L115

Handberg, R. & Lund, M. N. 2014, MNRAS, 445, 2698

Harvey, J. W. 1985, in Probing the depths of a star: the study of solar oscillations, ed. R. W. Noyes & E. J. Rhodes, Vol. 400, JPL, 327

Harvey, J. W., Hill, F., Hubbard, R., et al. 1996, Science, 272, 1284

Hekker, S., Broomhall, A., Chaplin, W. J., et al. 2010, MNRAS, 402, 2049

Hill, H. A., Stebbins, R. T., & Brown, T. M. 1976, Recent oblateness observations: Data, interpretation and significance for earlier work, ed. J. H. Sanders & A. H. Wapstra, Vol. 622-628 (Plenum Press)

Hill, H. A., Stebbins, R. T., & Oleson, J. R. 1975, ApJ, 200, 484

Houdek, G., Balmforth, N. J., Christensen-Dalsgaard, J., & Gough, D. O. 1999, A&A, 351, 582

Howe, R., Davies, G. R., Chaplin, W. J., Elsworth, Y. P., & Hale, S. J. 2015, ArXiv 1509.06894

Howell, S. B., Rowe, J. F., Bryson, S. T., et al. 2012, ApJ, 746, 123

Howell, S. B., Sobeck, C., Haas, M., et al. 2014, PASP, 126, 398

Huber, D., Bedding, T. R., Stello, D., et al. 2011, ApJ, 743, 143

Huber, D., Chaplin, W. J., Christensen-Dalsgaard, J., et al. 2013, ApJ, 767, 127

Huber, D., Stello, D., Bedding, T. R., et al. 2009, Communications in Asteroseismology, 160, 74

Jenkins, J. M., Caldwell, D. A., Chandrasekaran, H., et al. 2010, ApJ Lett., 713, L87

Jiménez-Reyes, S. J., García, R. A., Jiménez, A., & Chaplin, W. J. 2003, ApJ, 595, 446

Kaiser, M. L., Kucera, T. A., Davila, J. M., et al. 2008, Space Sci. Rev., 136, 5

Kallinger, T., De Ridder, J., Hekker, S., et al. 2014, A&A, 570, A41

Kallinger, T., Hekker, S., Mosser, B., et al. 2012, A&A, 541, A51

Karoff, C., Metcalfe, T. S., Chaplin, W. J., et al. 2009, MNRAS, 399, 914

Kjeldsen, H. & Bedding, T. R. 1995, A&A, 293, 87

Kjeldsen, H., Bedding, T. R., Baldry, I. K., et al. 2003, AJ, 126, 1483

Kjeldsen, H., Bedding, T. R., Viskum, M., & Frandsen, S. 1995, AJ, 109, 1313

Koch, D. G., Borucki, W. J., Basri, G., et al. 2010, ApJ Lett., 713, L79

Komm, R. W., Gu, Y., Hill, F., Stark, P. B., & Fodor, I. K. 1999, ApJ, 519, 407

Lazrek, M., Baudin, F., Bertello, L., et al. 1997, Sol. Phys., 175, 227

Lefebvre, S., García, R. A., Jiménez-Reyes, S. J., Turck-Chièze, S., & Mathur, S. 2008, A&A, 490, 1143

Leibacher, J. W. & Stein, R. F. 1971, Astrophys. Lett., 7, 191

Leighton, R. B., Noyes, R. W., & Simon, G. W. 1962, ApJ, 135, 474

Libbrecht, K. G. 1992, ApJ, 387, 712

Lopes, I. & Turck-Chièze, S. 1994, A&A, 290, 845

Lund, M. N., Kjeldsen, H., Christensen-Dalsgaard, J., Handberg, R., & Silva Aguirre, V. 2014, ApJ, 782, 2

Marigo, P., Girardi, L., Bressan, A., et al. 2008, A&A, 482, 883

Mathur, S., Bruntt, H., Catala, C., et al. 2013a, A&A, 549, A12

Mathur, S., Eff-Darwich, A., García, R. A., & Turck-Chièze, S. 2008, A&A, 484, 517

Mathur, S., García, R. A., Ballot, J., et al. 2014a, A&A, 562, A124

Mathur, S., García, R. A., Catala, C., et al. 2010a, A&A, 518, A53

Mathur, S., García, R. A., Morgenthaler, A., et al. 2013b, A&A, 550, A32

Mathur, S., García, R. A., Régulo, C., et al. 2010b, A&A, 511, A46

Mathur, S., Handberg, R., Campante, T. L., et al. 2011a, ApJ, 733, 95

Mathur, S., Hekker, S., Trampedach, R., et al. 2011b, ApJ, 741, 119

Mathur, S., Metcalfe, T. S., Woitaszek, M., et al. 2012, ApJ, 749, 152

Mathur, S., Salabert, D., García, R. A., & Ceillier, T. 2014b, Journal of Space Weather and Space Climate, 4, A15

Mathur, S., Turck-Chièze, S., Couvidat, S., & García, R. A. 2007, ApJ, 668, 594

Matthews, J. M., Kuschnig, R., Walker, G. A. H., et al. 2000, in Astronomical Society of the Pacific Conference Series, Vol. 203, IAU Colloq. 176: The Impact of Large-Scale Surveys on Pulsating Star Research, ed. L. Szabados & D. Kurtz, 74–75

Metcalfe, T. S., Basu, S., Henry, T. J., et al. 2010, ApJ Lett., 723, L213

Metcalfe, T. S., Chaplin, W. J., Appourchaux, T., et al. 2012, ApJ Lett., 748, L10

Michel, E., Samadi, R., Baudin, F., et al. 2009, A&A, 495, 979

Mosser, B. & Appourchaux, T. 2009, A&A, 508, 877

Mosser, B., Barban, C., Montalbán, J., et al. 2011, A&A, 532, A86

Mosser, B., Baudin, F., Lanza, A. F., et al. 2009a, A&A, 506, 245

Mosser, B., Bouchy, F., Catala, C., et al. 2005, A&A, 431, L13

Mosser, B., Elsworth, Y., Hekker, S., et al. 2012a, A&A, 537, A30

Mosser, B., Goupil, M. J., Belkacem, K., et al. 2012b, A&A, 540, A143

Mosser, B., Michel, E., Appourchaux, T., et al. 2009b, A&A, 506, 33

Moya, A., Amado, P. J., Barrado, D., et al. 2010, MNRAS, 406, 566

Murphy, S. J., Shibahashi, H., & Kurtz, D. W. 2013, MNRAS, 430, 2986

Musman, S. 1974, Sol. Phys., 36, 313

Nigam, R. & Kosovichev, A. G. 1998, ApJ Lett., 505, L51

Osaki, J. 1975, PASJ, 27, 237

Pallé, P. L., Appourchaux, T., Christensen-Dalsgaard, J., & García, R. A. 2015, Extraterrestrial Seismology, ed. V. C. H. Tong & R. A. García (Cambridge University Press)

Percival, D. B. & Walden, A. T. 1993, Spectral Analysis for Physical Applications

Pires, S., Mathur, S., García, R. A., et al. 2015, A&A, 574, A18

Poppenhaeger, K. & Schmitt, J. H. M. M. 2011, ApJ, 735, 59

Press, W. H. & Rybicki, G. B. 1989, ApJ, **338**, 277

Press, W. H., Teukolsky, S. A., Vetterling, W. T., & Flannery, B. P. 1992, Numerical recipes in FORTRAN. The art of scientific computing (Cambridge: University Press, —c1992, 2nd ed.)

Rauer, H., Catala, C., Aerts, C., et al. 2014, Experimental Astronomy, 38, 249

Ricker, G. R., Winn, J. N., Vanderspek, R., et al. 2014, in Society of Photo-Optical Instrumentation Engineers (SPIE) Conference Series, Vol. 9143, Society of Photo-Optical Instrumentation Engineers (SPIE) Conference Series, 20

Roberts, D. H., Lehar, J., & Dreher, J. W. 1987, AJ, 93, 968

Roca Cortés, T., Jiménez, A., Pallé, P. L., GOLF team, & VIRGO Team. 1999, in ESA Special Publication, Vol. 448, Magnetic Fields and Solar Processes, ed. A. Wilson & et al., 135

Roxburgh, I. W. & Vorontsov, S. V. 2003, A&A, 411, 215

Roxburgh, I. W. & Vorontsov, S. V. 2007, MNRAS, 379, 801

Salabert, D., Ballot, J., & García, R. A. 2011a, A&A, 528, A25

Salabert, D., García, R. A., Pallé, P. L., & Jiménez-Reyes, S. J. 2009, A&A, 504, L1

Salabert, D., García, R. A., & Turck-Chièze, S. 2015, A&A, 578, A137

Salabert, D., Régulo, C., Ballot, J., García, R. A., & Mathur, S. 2011b, A&A, 530, A127

Samadi, R., Belkacem, K., Ludwig, H.-G., et al. 2013, A&A, 559, A40

Samadi, R., Fialho, F., Costa, J. E. S., et al. 2007, ArXiv 0703354

Scargle, J. D. 1982, ApJ, 263, 835

Scherrer, P. H., Bogart, R. S., Bush, R. I., et al. 1995, Sol. Phys., 162, 129

Scuflaire, R., Gabriel, M., Noels, A., & Boury, A. 1975, A&A, 45, 15

Silva Aguirre, V., Casagrande, L., Basu, S., et al. 2012, ApJ, 757, 99

Silva Aguirre, V., Davies, G. R., Basu, S., et al. 2015, MNRAS, 452, 2127

Slepian, D. 1978, AT T Technical Journal, 57, 1371

Soriano, M. & Vauclair, S. 2010, A&A, 513, A49

Stello, D., Bruntt, H., Kjeldsen, H., et al. 2007, MNRAS, 377, 584

Stello, D., Chaplin, W. J., Bruntt, H., et al. 2009, ApJ, 700, 1589

Stello, D., Huber, D., Bedding, T. R., et al. 2013, ApJ Lett., 765, L41

Stello, D., Huber, D., Sharma, S., et al. 2015, ApJ Lett., 809, L3

Stello, D., Meibom, S., Gilliland, R. L., et al. 2011, ApJ, 739, 13

Tanenbaum, A. S., Wilcox, J. M., Franzier, E. N., & Howard, R. 1969, Sol. Phys., 9, 328

Thiery, S., Boumier, P., Gabriel, A. H., et al. 2000, A&A, 355, 743

Thompson, M. J., Toomre, J., Anderson, E., et al. 1996, Science, 272, 1300

Thompson, S. E., Christiansen, J. L., Jenkins, J. M., et al. 2013, Kepler Data Release 21 Notes (KSCI-19061-001), Kepler mission

Thomson, D. J. 1982, IEEE Proceedings, 70, 1055

Thuillier, G., Dewitte, S., & Schmutz, W. 2006, in 36th COSPAR Scientific Assembly, 170

Toutain, T., Appourchaux, T., Fröhlich, C., et al. 1998, ApJ Lett., 506, L147

Turck-Chièze, S., Basu, S., Brun, A. S., et al. 1997, Sol. Phys., 175, 247

Turck-Chièze, S., Couvidat, S., Kosovichev, A. G., et al. 2001, ApJ Lett., 555, L69

Turck-Chièze, S., Däppen, W., Fossat, E., et al. 1993, Phys. Rep., 230, 57

Turck-Chièze, S., García, R. A., Couvidat, S., et al. 2004, ApJ, 604, 455

Ulrich, R. K. 1970, ApJ, 162, 993

Unno, W., Osaki, Y., Ando, H., Saio, H., & Shibahashi, H. 1989, Nonradial oscillations of stars

Vauclair, S. 2011, in IAU Symposium, Vol. 276, IAU Symposium, ed. A. Sozzetti, M. G. Lattanzi, & A. P. Boss, 30–33

Vázquez Ramió, H., Roca Cortés, T., & Régulo, C. 2002, in ESA Special Publication, Vol. 506, Solar Variability: From Core to Outer Frontiers, ed. A. Wilson, 897–900

Vorontsov, S. V., Baturin, V. A., & Pamiatnykh, A. A. 1991, Nature, 349, 49

Weiss, W. W., Rucinski, S. M., Moffat, A. F. J., et al. 2014, PASP, 126, 573

Woodard, M. F. & Noyes, R. W. 1985, Nature, 318, 449

Zahn, J., Brun, A., & Mathis, S. 2008, in SF2A-2008, ed. C. Charbonnel, F. Combes, & R. Samadi, 341